

Modular MPS_3 -Based Frameworks for Superionic Conduction of Monovalent and Multivalent Ions

Zachery W. B. Iton,[†] Zion Irving-Singh,[‡] Son-Jong Hwang,[‡] Amit Bhattacharya,[¶] Sammy Shaker,[§] Tridip Das,^{||} Raphaële J. Clément,[¶] William A. Goddard III,^{||} and Kimberly A. See^{*,‡}

[†]*Department of Applied Physics and Materials Science, California Institute of Technology, Pasadena, California 91125, United States*

[‡]*Division of Chemistry and Chemical Engineering, California Institute of Technology, Pasadena, California 91125, United States*

[¶]*Materials Department and Materials Research Laboratory, University of California, Santa Barbara, Santa Barbara, California 93106, United States*

[§]*Division of Biology and Biological Engineering, California Institute of Technology, Pasadena, CA 91125, United States*

^{||}*Materials and Process Simulation Center (MSC), California Institute of Technology, Pasadena, California 91125, United States*

Received May 4, 2024; E-mail: ksee@caltech.edu

Abstract: Next-generation batteries based on more sustainable working ions could offer improved performance, safety, and capacity over lithium-ion batteries, while also decreasing the cost. Development of next-generation battery technology using "beyond-Li" mobile ions is limited, in part, due to a lack of understanding of solid state conduction of these ions. Next-generation mobile ions tend to have relatively low mobility in solids due to: (1) larger ionic radii (Na^+ , K^+ , Ca^{2+}), which limit the accessible migration pathways, and/or (2) higher charge densities (Mg^{2+} , Zn^{2+} , Al^{3+}), which result in strong electrostatic interactions within the solid. Here, we introduce ligand-coordinated ions into MPS_3 -based solid host crystals ($M = Mn, Cd$) to simultaneously increase the size of the bottlenecks within the migration pathway and screen the charge-dense ions. We employ X-ray diffraction, thermogravimetric analysis, inductively coupled plasma mass spectrometry, scanning electron microscopy, energy dispersive X-ray spectroscopy, solid state magic angle spinning nuclear magnetic resonance spectroscopy, pulsed field gradient nuclear magnetic resonance spectroscopy, density functional theory quantum mechanics, and electrochemical impedance spectroscopy to probe the ionic mobility, structural and chemical changes in the MPS_3 materials after ion exchange.

We show that the inclusion of coordinating ligands enables ambient temperature superionic conductivity of various next-generation mobile ions in an electronically-insulating MPS_3 -based solid. These ion-intercalated MPS_3 -based frameworks not only enable deeper understanding of ligand-coordination in solid state ionic conduction, but could potentially serve as a universal solid state electrolyte for various next-generation battery chemistries.

Introduction

The landscape of modern battery technology has been dominated by lithium-ion batteries (LIBs). However, material availability, scalability, cost, and escalating global energy demands,¹⁻³ motivate development of alternative battery chemistries. "Next-generation" mobile ions, such as Na^+ , K^+ , Mg^{2+} , Ca^{2+} , Zn^{2+} , and Al^{3+} ,

represent a promising frontier in battery technology due to their abundance and potential for high volumetric capacities.⁴ However, one of the major challenges in developing battery technology based on next-generation mobile ions is the difficulty in achieving solid state conduction of those ions. Solid state conduction is crucial for ion transport in electrodes, interphases, and solid electrolytes. The larger size of ions like Na^+ , K^+ , Ca^{2+} restrict their movement through the typically rigid migration pathways available in solid materials. Additionally, the mobility of ions with higher charge densities, such as Mg^{2+} , Zn^{2+} , Al^{3+} , is impeded by the strong electrostatic interactions between these mobile ions and other ions within the solid. These challenges are outlined in detail in our recent perspective.⁴ Difficulties with solid state ionic conduction are less pronounced in Li-based systems due to the relatively small size and low charge density of Li^+ .

Solid state conduction of larger cations has typically been achieved in structures based on open frameworks with large migration bottlenecks, like Prussian blue analogues,⁵⁻⁷ β -Alumina,⁸⁻¹¹ or NASICON phases.¹²⁻¹⁴ Whereas, solid state conduction of charge-dense ions has been mostly limited to electronically-conductive materials. In systems like Mo_6S_8 , thiospinel Ti_2S_4 , and $MgSc_2S_4$, the mobile electrons are hypothesized to facilitate ionic mobility by screening the charge-dense ions, decreasing the strength of electrostatic interactions within the solid.¹⁵⁻¹⁹ For electronically-insulating materials, such as solid electrolytes or interphases, there is an absence of mobile electrons to screen the charge of the targeted ions. Only a handful of electronically-insulating inorganic solids have been shown to conduct charge-dense ions, such as Zn^{2+} in $ZnPS_3$,²⁰ or Mg^{2+} in borohydrides,²¹⁻²⁶ but each have their own challenges associated with low room temperature conductivities (σ_{RT}) or high activation energy (E_a).

One path to enable the conduction of large or charge-dense cations in electronic insulators is to introduce ligands, like H_2O , that can coordinate to the targeted cations within the host crystal. Solid state mobility of ligand-coordinated ions was extensively studied in mica clays such as vermiculite and montmorillonite.²⁷⁻³¹ However, in clays the σ is generally $< 0.1 \text{ mS cm}^{-1}$. In battery systems, the addition of H_2O to increase multivalent ionic conduction has been primarily attempted for cathode materials, such as MnO_2 and V_2O_5 .³²⁻³⁵ Recently, this concept has been extended to electronically-insulating inorganic solids, like $Li_2Sn_2S_5$ ³⁶ and $ZnPS_3$,³⁷ as well as various MOFs and COFs,³⁸⁻⁴² for solid state

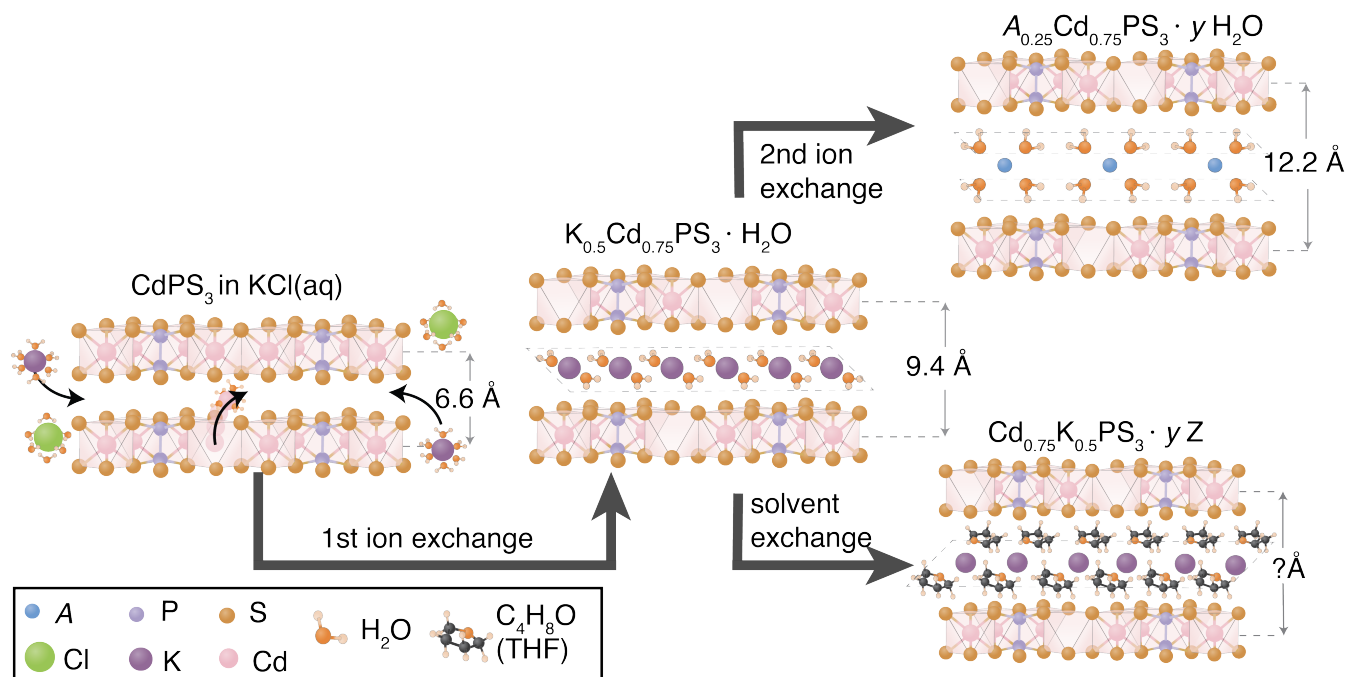


Figure 1. A schematic of the ion and ligand exchange used in the present study. In an aqueous KCl solution, CdPS₃ intercalates hydrated K⁺ ions into the van der Waals gap and maintains charge neutrality by losing Cd²⁺ ions from the metal layer. After K_{0.5}Cd_{0.75}PS₃ is formed one can perform either: (1) a second ion exchange to introduce desired monovalent or multivalent mobile ions, or (2) a ligand exchange to replace H₂O in the system.

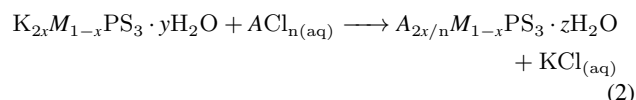
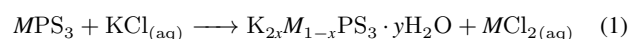
electrolyte applications.

Here, we leverage coordinated ligand molecules within solid frameworks based on MPS₃ materials (*M* = Mn, Cd) to achieve two primary goals: (1) increasing the size of the bottlenecks in migration pathways and (2) screening charge-dense ions to decrease electrostatic interactions within the lattice. By combining the advantages of large bottlenecks and charge screening we can devise a universal framework for ambient temperature superionic conduction of various ions within an inorganic, electronically-insulating solid.

CdPS₃ and MnPS₃ exhibit a peculiar mechanism for the intercalation of hydrated cations into the van der Waals gap.⁴³ Unlike the redox-based intercalation in common battery electrodes in which incorporation of a cation coincides with a Faradaic reduction of the host,⁴⁴ when cations are intercalated into MPS₃ materials, charge balance is maintained by M²⁺ loss in an ion exchange mechanism.^{43,45,46} This mechanism is similar to that observed in clays.^{27,28,47,48} CdPS₃ and MnPS₃ form as monoclinic (C2/m) layered compounds with a slightly distorted hexagonal network of edge-sharing Cd²⁺ or Mn²⁺ octahedra. The Cd²⁺ or Mn²⁺ are coordinated by [P₂S₆]⁴⁻ polyanions. The layers stack along the *c*-axis separated by a van der Waals gap of ~ 3.5 Å.⁴⁹ The basal spacing (*d*₍₀₀₁₎) of CdPS₃ is slightly larger than that of MnPS₃ (6.55 vs. 6.49 Å) due to the larger size of Cd²⁺ over Mn²⁺ (0.95 vs. 0.83 Å).⁵⁰

Here, we exploit the ability of CdPS₃ and MnPS₃ to host cations within the van der Waals gap to generate materials that contain various ions of interest through a sequential ion exchange strategy that is illustrated in Figure 1. First, a cation with a small hydrated radius (e.g. K⁺) is intercalated into the van der Waals gap of an MPS₃ material.⁴⁵ Charge neutrality is maintained through the loss of the labile metal (Cd²⁺ or Mn²⁺) from the metal layer (Equation 3), resulting in negatively charged sheets of MPS₃ sandwiching positively charged, hydrated ions. The hydrated K⁺ ions can be further exchanged to introduce a larger hydrated cation (*A*), like Li⁺, Na⁺, Mg²⁺, Ca²⁺, Zn²⁺, Al³⁺ (Equation 2). Direct insertion of large

hydrated cations is kinetically limited, as such this sequential exchange method is preferred.



Additionally, we demonstrate that the H₂O molecules can be exchanged for aprotic ligands, e.g. acetonitrile (MeCN), and tetrahydrofuran (THF). The ligand exchange serves several purposes: (1) to probe the effect of different ligand molecules on ionic mobilities, (2) to demonstrate that the mobile ions conduct in the absence of H⁺, and (3) to broaden the applicability of these frameworks to H₂O-incompatible systems.

The ability of MPS₃ materials to intercalate a wide variety of guest ions and molecules has been useful for diverse applications. The areas of research span from non-linear optics,^{51,52} photoluminescence,⁵³ hosts for biomolecules⁵⁴ or polymers,^{55,56} and superconducting magnets.⁵⁷ However, the ionic conductivity of these materials has been less rigorously explored. Some studies have investigated the mobility of hydrated Na⁺, K⁺, and Cs⁺ in CdPS₃.⁵⁸⁻⁶¹ These studies concluded that Na⁺ was slightly mobile (10⁻⁵ S cm⁻¹) but K⁺ and Cs⁺ were immobile. Another study investigated the conductivity of trivalent cations in MPS₃ in the dried state, finding no significant ionic conduction (10⁻⁸ – 10⁻¹⁰ S cm⁻¹).⁶² Notably, nanosheet-based membranes using Cd_{0.85}PS₃Li_{0.15}H_{0.15} were found to have exceedingly high 2D H⁺ conductivity (300 mS cm⁻¹ at RT and 98 % relative humidity (RH)).⁶³

Recently, Yu & Ren reported on CdPS₃-based nanosheet membranes with various intercalated cations.⁶⁴ The membranes boasted impressive 2D ionic conductivity but importantly, the conductivity was similar irrespective of the intercalated cation (170–

Table 1. The stoichiometry of each $A_{2x/n}M_yPS_3$ compound, x and y are measured by ICP-MS and normalized to P, which is assumed to be constant. The H_2O content of each compound, which is determined with a combination of TGA and measured mass pre- and post-drying using an analytical balance. The amount of H_2O per intercalated ion in each material, and the nominal formula of each compound based on the measured cation content.

Compound	x	y	$H_2O/f.u.$	H_2O/A	Nominal Formula
$K_xCd_yPS_3$	0.50 ± 0.02	0.79 ± 0.02	1.0 ± 0.1	2	$K_{0.5}Cd_{0.75}PS_3 \cdot H_2O$
$Li_xCd_yPS_3$	0.47 ± 0.01	0.85 ± 0.03	2.0 ± 0.7	4.4	$Li_{0.5}Cd_{0.75}PS_3 \cdot 2 H_2O$
$Na_xCd_yPS_3$	0.51 ± 0.02	0.81 ± 0.02	2.0 ± 0.5	3.9	$Na_{0.5}Cd_{0.75}PS_3 \cdot 2 H_2O$
$Mg_xCd_yPS_3$	0.24 ± 0.01	0.78 ± 0.05	1.9 ± 0.0	7.9	$Mg_{0.25}Cd_{0.75}PS_3 \cdot 1.9 H_2O$
$Ca_xCd_yPS_3$	0.24 ± 0.02	0.81 ± 0.02	2.0 ± 0.5	8.3	$Ca_{0.25}Cd_{0.75}PS_3 \cdot 2 H_2O$
$Zn_xCd_yPS_3$	0.41 ± 0.09	0.76 ± 0.24	0.25	0.63	$Zn_{0.4}Cd_{0.6}PS_3 \cdot 0.25 H_2O$
$Al_xCd_yPS_3$	0.13 ± 0.01	0.81 ± 0.08	2.5 ± 0.6	14.5	$Al_{0.17}Cd_{0.75}PS_3 \cdot 2.3 H_2O$
$K_xMn_yPS_3$	0.40 ± 0.05	0.80 ± 0.03	0.8 ± 0.2	2.1	$K_{0.4}Mn_{0.8}PS_3 \cdot 0.8 H_2O$
$Li_xMn_yPS_3$	0.34 ± 0.03	0.84 ± 0.03	1.4 ± 0.2	4.0	$Li_{0.4}Mn_{0.8}PS_3 \cdot 1.4 H_2O$
$Na_xMn_yPS_3$	0.59 ± 0.08	0.71 ± 0.04	1.7 ± 0.6	2.7	$Na_{0.6}Mn_{0.7}PS_3 \cdot 1.7 H_2O$
$Mg_xMn_yPS_3$	0.19 ± 0.01	0.82 ± 0.01	1.8 ± 0.1	9.5	$Mg_{0.2}Mn_{0.8}PS_3 \cdot 1.8 H_2O$
$Ca_xMn_yPS_3$	0.25 ± 0.02	0.76 ± 0.02	1.5 ± 0.1	6	$Ca_{0.25}Mn_{0.75}PS_3 \cdot 1.5 H_2O$
$Zn_xMn_yPS_3$	0.46 ± 0.06	0.62 ± 0.06	1.6 ± 0.1	2.6	$Zn_{0.4}Mn_{0.6}PS_3 \cdot 1.6 H_2O$
$Al_xMn_yPS_3$	0.12 ± 0.00	0.84 ± 0.01	2.4 ± 0.4	16	$Al_{0.13}Mn_{0.8}PS_3 \cdot 2.2 H_2O$

330 $mS\ cm^{-1}$ at RT and 98 % RH). In fact, the ion-intercalated membranes also displayed similar behavior in regards to layer expansion and activation energy. This is likely due to excess H_2O content within the restacked membranes which could lead to significant contribution from H^+ conduction through a Grotthuss mechanism,^{63,65} or direct diffusion of solvated ions in a confined liquid electrolyte. Such a mechanism is distinct to conduction of ligand-coordinated ions within a host crystal. The transition from ligand-coordinated solid state conduction to the conduction of solvated ions within a confined liquid in the solid framework at excess ligand/solvent concentrations has been noted in previous studies of hydrated $Li_2Sn_2S_5$, MOFs, and clays.^{36,66–68}

To minimize contributions from H^+ conduction and to reveal inherent structure-property relationships that can be drowned out in the presence of excess H_2O , here we investigate bulk, ion-intercalated $CdPS_3$ and $MnPS_3$ materials primarily at ambient RH (~ 40 – 55 %), and with coordinating ligands that range from H_2O to aprotic, neutral solvent molecules. This allows us to understand the nuanced differences between the effects of various frameworks, intercalated ions, and coordinating ligands on the ionics thereby deepening our understanding of ionic conduction in solids. Additionally, the 3D bulk conduction pathways in polycrystalline samples in this study are directly applicable to practical battery applications. We also introduce $MnPS_3$ as an environmental friendly alternative with comparable performance, and demonstrate non-aqueous analogues that would be more compatible with desirable electrode materials.

We employ several characterization techniques to study the structural and chemical changes after ion exchange, as well as the resulting ionic mobility. These techniques include: electrochemical impedance spectroscopy (EIS), X-ray diffraction (XRD), thermogravimetric analysis (TGA), inductively coupled plasma mass spectrometry (ICP-MS), scanning electron microscopy (SEM), energy dispersive X-ray spectroscopy (EDS), quantum mechanics simulations, solid state magic angle spinning nuclear magnetic resonance spectroscopy (MAS NMR), and pulsed field gradient nuclear magnetic resonance spectroscopy (PFG NMR). At ambient temperature and RH, all of the H_2O -coordinated interlayer cations, barring Al^{3+} -intercalated $MnPS_3$, exhibit "superionic", or practically useful, bulk conductivity ($> 0.1\ mS\ cm^{-1}$) and relatively low E_a . Notably, in the polycrystalline samples studied here both σ_{RT} and E_a vary significantly depending on the identity of the intercalated cation. The ligand exchange to aprotic molecules generally results in decreased σ_{RT} and increased E_a , but achieving practically useful

conductivity is still possible using ligands like MeCN.

Results and Discussion

Chemical and Structural Characterization After Ion Exchange

Elemental Analysis

MPS_3 materials can undergo ion exchange processes as outlined in Equations 3 and 2. The ion exchanges have been well characterized in previous reports.^{45,52} However, the amount of M that is replaced by A , described by ' x ' in Equations 3 and 2, differs between various studies – ranging from $0.1 \leq x \leq 0.25$.^{43,52,60,64} Intuitively, x can be controlled by varying the $MPS_3:ACl_{n(aq)}$ ratio, as illustrated in Figure S1. Here, we aimed for high A content ($x \simeq 0.25$ for $CdPS_3$ -based samples and $\simeq 0.20$ for $MnPS_3$ -based samples) to incorporate the largest number of charge carriers, which we hypothesize will lead to optimal conductivity. Table 1 shows the results of elemental analysis on the ion-intercalated MPS_3 compounds. The amount of A intercalated (x) and remaining M (y) are determined using ICP-MS and are normalized to the measured P content. The measured S content is inaccurate due to H_2S evolution during the sample digestion process, but it is also presumed to stay constant. The standard deviations for the ICP-MS data are representative of a minimum of five different synthesis batches per material. Due to synthesis and measurement inaccuracies the precise stoichiometry of the $A_{2x/n}Cd_{1-x}PS_3$ compounds sometimes contains $\leq 10\%$ excess Cd, however a comparison of "ideal" batches and those with excess Cd shows that there is no noticeable impact on the σ_{RT} and E_a (Figure S2). The H_2O content is determined by a combination of TGA (Figure S3) and changes in pellet masses pre- and post-drying, measured using an analytical balance. For the rest of this manuscript, the compounds are referred to by their nominal formula for simplicity. The differences in the degree of ion exchange that occurs, both for different ions within a given framework and between the frameworks ($CdPS_3$ vs. $MnPS_3$), is discussed in Supplementary Note 1.

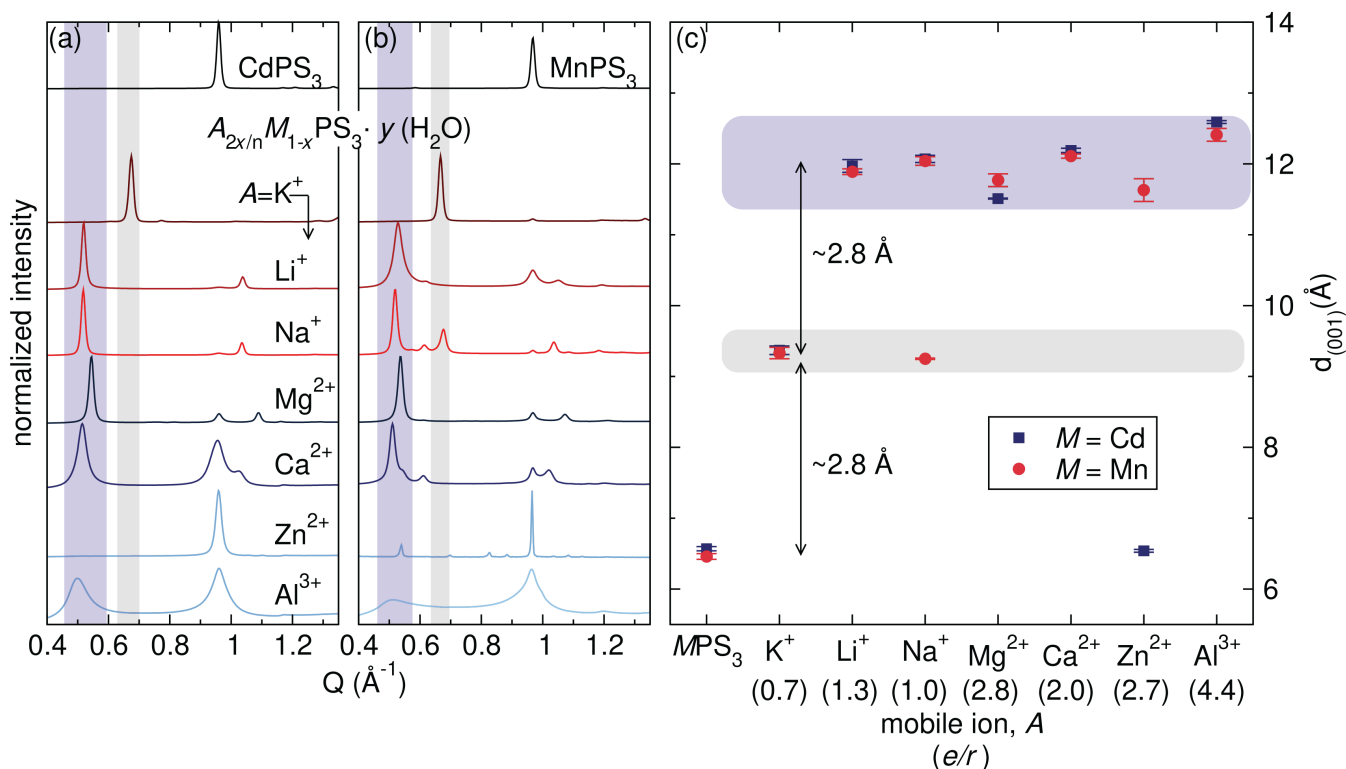


Figure 2. Characterization of the $A_{2x/n}M_{1-x}PS_3 \cdot y H_2O$ materials using powder XRD. XRD patterns of (a) CdPS₃-based and (b) MnPS₃-based compounds. (c) $d_{(001)}$ spacing of $A_{2x/n}M_{1-x}PS_3 \cdot y H_2O$. The error bars reflect the standard deviation of several XRD measurements, the differences are due to the range of ambient humidity ($\approx 40\text{-}55\%$). The gray regions highlight materials with a monolayer of H₂O and the purple regions highlight materials with a bilayer of H₂O. Note, the pattern of Zn_{0.4}Mn_{0.6}PS₃ · 1.6 H₂O is collected using Cu K α radiation because the sample inadvertently dehydrated during preparation for the synchrotron measurement.

Experimental Structural Investigation

The changes to the crystal structure of the MPS₃ materials after ion exchange is investigated using XRD. Figure 2a and b show the low Q regions of representative XRD patterns of ion-exchanged CdPS₃-based and MnPS₃-based compounds, respectively, to highlight the layer spacing. Full XRD patterns are shown in Figure S4. After ion exchange, all of the materials are vacuum filtered until dry and then equilibrated at ambient RH before XRD is taken. Previous work has confirmed that the structure within the metal layers is maintained upon ion exchange.^{52,58,69} Raman spectra are measured for the CdPS₃-based compounds to confirm that the polyanion remains intact and its environment in the metal layer is largely unchanged (Figure S5).

Figure 2c shows the extracted $d_{(001)}$ values for all compounds. Error bars are shown to reflect the deviation associated with fluctuating RH at the time of replicate measurements. The original (001) reflection of the pristine MPS₃ phase occurs at $Q = 0.95$ and 0.97 for $M = Cd$ and Mn , respectively. The expanded (001) reflection of the ion-exchanged materials appears between $Q = 0.49$ and 0.67 Å and the subsequent (002) reflections can be seen around $Q \approx 1.05$ Å. Layer expansion suggests incorporation of the ions into the van der Waals gap and SEM confirms that the layered platelet morphology of the particles is maintained. EDS confirms that the intercalated ions are homogeneously dispersed within the particles (Figure S6).

It is clear from Figure 2c that the $d_{(001)}$ spacing after ion exchange can be grouped into two main categories. The layer spacing of the hydrated structures increases by either ~ 2.8 Å or ~ 5.6 Å. These expansions correspond to the van der Waals radius of one or two H₂O molecules, respectively. Therefore, the layer spacing increase is likely due to the formation of either a monolayer or bilayer

of H₂O around the intercalated cations in the van der Waals gap, rather than following the expected hydrated cation radii of the inserted ions. The formation of hydrated MPS₃ materials containing mono or bilayer H₂O has been noted in previous works on monovalent cation intercalated MPS₃ materials.^{45,52,60} However, to the best of our knowledge, the hydrated structure of MPS₃ phases containing other ions has not been explored.

The occurrence of mono or bilayer H₂O structures with the other ions is similar to the results in clays, transition metal dichalcogenides (MS₂), or MXenes, which also exhibit hydrated structures containing mono or bilayer H₂O with a wide range of interlayer cations.^{28,67,70–73}

Whittingham, in addition to Lerb and Schöllhorn, independently investigated the hydration of interlayer ions in MS₂ compounds, ($M = Ti, Nb, Ta$).^{71,72} These studies showed that the resulting structure of the hydrated compounds is governed by the cation-ligand interaction. Specifically, the ability of the cation-ligand interaction to offset the loss in electrostatic lattice energy incurred by separating the cations from the anionic sulfide layers. Lerb and Schöllhorn found that this behavior can be described empirically by the charge/radius ratio (e/r) of the interlayer cations, which is correlated with the hydration energy. These rules translated well to other layered hydrated structures, like MXenes.⁷³ Cations for which $e/r < 1$ (large and low charge, e.g. K⁺) can only stabilize a monolayer of H₂O, whereas if $e/r > 1$ (small and high charge, e.g. Li⁺ and multivalents) then a bilayer of H₂O can be stabilized. In Figure 2c, we show the e/r value for each mobile ion and confirm the relationship between e/r and the layer spacing in the ion-intercalated MPS₃ materials. The e/r of Na⁺ is ≈ 1 , suggesting that it can stabilize either a monolayer or bilayer of H₂O. Indeed, isolated forms of monolayer or bilayer H₂O, or even a mixture of both, can be

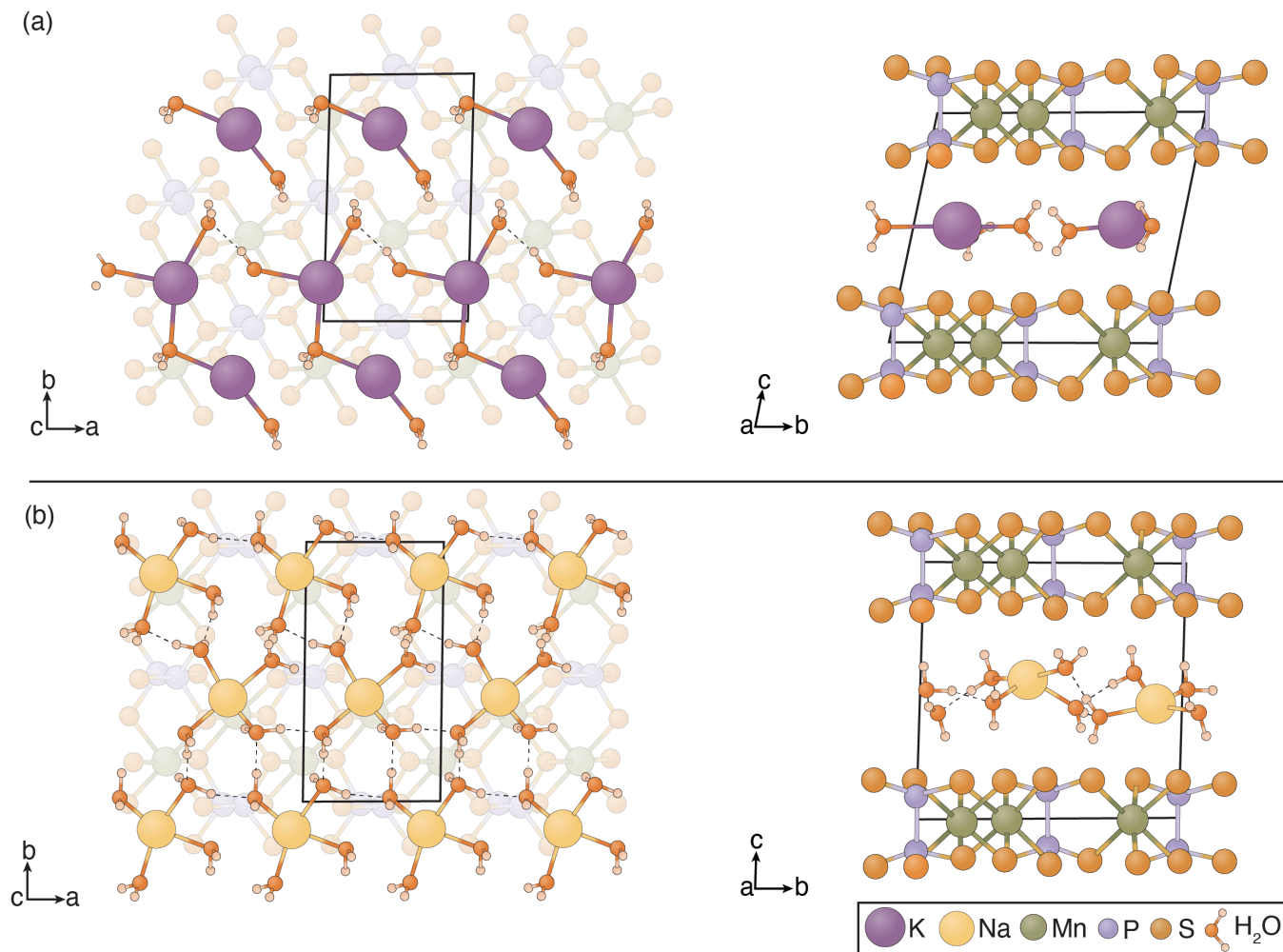


Figure 3. Computationally relaxed structures of (a) $\text{K}_{0.5}\text{Mn}_{0.75}\text{PS}_3 \cdot \text{H}_2\text{O}$ and (b) $\text{Na}_{0.5}\text{Mn}_{0.75}\text{PS}_3 \cdot 2 \text{H}_2\text{O}$. The left images show the view down the c axis after removing the metal layer above the hydrated interlayer cations, the metal layer below is made partially transparent for clarity. The right images show the view down the a axis. Hydrogen bonds between H_2O molecules are shown as dotted black lines. The H_2O molecules are inaccurately depicted as being smaller than the interlayer cation for clarity.

achieved when $A = \text{Na}^+$ depending on the RH (Figure S7). Furthermore, the TGA and derivative thermogravimetry (DTG) results (Figure S3) show that $\text{Na}_{0.5}\text{Cd}_{0.75}\text{PS}_3 \cdot 2 \text{H}_2\text{O}$ is the only CdPS_3 -based compound with two distinct H_2O loss events, corresponding to the transition between the stable monolayer and bilayer H_2O structures. The H_2O content of materials containing multivalents, e.g. $\text{Ca}_{0.25}\text{Mn}_{0.75}\text{PS}_3$, changes as the RH is varied but a phase transition to a structure with monolayer H_2O is not observed for multivalent intercalated compounds at any RH due to the higher hydration energies of the multivalent ions. The solvation shells of multivalent ions are likely incomplete at low RH, but the overall bilayer structure is maintained (Figure S8). This also agrees with the findings of Lerf and Schöllhorn for MS_2 compounds.⁷¹ Notably, in contrast to the structure observed by Yu *et al.* in CdPS_3 -based membranes,⁶⁴ bulk $\text{K}_{0.5}\text{Cd}_{0.75}\text{PS}_3$ could not be forced into a bilayer H_2O structure even at 96 % RH (Figure S9), perhaps due to the more rigid constraints of the polycrystalline powders.

Structural Effects Associated with the Mobile Ion

Next, we consider the structural effects associated with (1) the identity of the mobile ion and (2) the CdPS_3 vs. the MnPS_3 host structure. First, we consider the structure of a given MPS_3 framework with different ions. As outlined above, of the ions selected for this

study only K^+ stabilizes a hydrated structure with a monolayer of H_2O , while the other ions stabilize a bilayer at ambient RH in both MPS_3 -based frameworks. Although two main categories of layer spacings exist as the mobile ion is changed, there is a measurable deviation of the layer spacing within the bilayer regime depending on the intercalated cation. We plot the charge density of the mobile ion for structures that reside in the bilayer regime vs. the $d_{(001)}$ layer spacing (shown in Figure S10) and find that the layer spacing is inversely related to the charge density of the intercalated ions. More charge-dense ions, such as Mg^{2+} , interact more strongly with the H_2O ligands, creating shorter bonds and therefore, a smaller total diameter of the hydrated cation complex. Al^{3+} is an outlier in this trend likely because the very high charge density of the cation attracts more H_2O which expands the layer. In fact, the Al-containing material contains more mol equivalents of H_2O ($\sim 16:1 \text{ H}_2\text{O}:\text{Al}$) then can be accommodated in a first shell coordination environment. However, the H_2O does not behave as "free" water as evidenced by ^1H NMR (*vide infra*).

Ion exchange with Zn^{2+} in both structures behaves differently compared to most of the other ions. In both host materials, reflections associated with the pristine MPS_3 phase dominate the diffraction patterns, though a small peak associated with an expanded lattice is observed for the MnPS_3 framework. We note that Zn

is indeed incorporated into the materials (see Table 1). For the CdPS₃-based material, we interpret these data to mean that most of the Zn²⁺ prefers to occupy the vacancies in the metal layer, which would suggest that the material does not contain substantial ligand-coordinated Zn²⁺. Indeed, the Zn_{0.4}Cd_{0.6}PS₃ material does not contain a significant amount of H₂O (Table 1). The Zn_{0.6}Mn_{0.4}PS₃, which shows a small expanded reflection, does contain some water due to the small ligand-coordinated Zn²⁺ content. Zn²⁺ is thermodynamically stable in the metal layer as evidenced by the ZnPS₃, which is a stable endmember that is isostructural to CdPS₃ and MnPS₃.⁷

The Difference in Structural Changes Between Frameworks

Next, we discuss trends between CdPS₃ and MnPS₃ frameworks. A comparison of the two frameworks reveals that generally the CdPS₃-based compounds have a larger $d_{(001)}$ than the MnPS₃-based compounds, which is consistent with the pristine materials (Figure 2c). However, Mg_{0.2}Mn_{0.8}PS₃ · 1.8 H₂O has a larger basal spacing than Mg_{0.25}Cd_{0.75}PS₃ · 1.9 H₂O. At this time, we do not know why this is. Na_{0.6}Mn_{0.7}PS₃ · 1.6 H₂O forms a two phase mixture of mono and bilayer H₂O at ambient RH while only the bilayer is formed with the CdPS₃ host at ambient RH. Even though the Mn analogue has more intercalated Na⁺, it absorbs less H₂O at a given RH. This is likely because the smaller lattice of MnPS₃ demands a larger energy cost for expansion, therefore a higher driving force for H₂O absorption (i.e. higher RH) is required to stabilize the bilayer structure.

Density Functional Theory (DFT) Simulations

The stable monolayer hydrated structure of K_{0.5}Mn_{0.75}PS₃ · H₂O and bilayer hydrated structure of Na_{0.5}Mn_{0.75}PS₃ · 2 H₂O are investigated using DFT simulations to gain further insight into the organization of H₂O molecules and interlayer cations. Such information is difficult to obtain experimentally due to the lack of long range order of the interlayer cations and ligated H₂O – no superstructure peaks are observed in the diffraction. Figure 3a shows the relaxed structure of K_{0.5}Mn_{0.75}PS₃ · H₂O and 3b shows the relaxed structure of Na_{0.5}Mn_{0.75}PS₃ · 2 H₂O. The interlayer cation and H₂O organization is highlighted viewed down the *c* axis and down the *a* axis. In K_{0.5}Mn_{0.75}PS₃ · H₂O, some of the H₂O is bridging between two K⁺ ions, while the others are more isolated to one K⁺ ion. The isolated H₂O ligands are hydrogen bonded to neighbors and located approximately within the same *ab* plane, supporting the experimentally measured $d_{(001)}$ spacing that suggests roughly a monolayer of H₂O. Many other configurations of K_{0.5}Mn_{0.75}PS₃ · H₂O are similarly stable and are shown and discussed in Figure S11. The variety of possible structures explains the lack of K ordering in the experimental data with multiple possible configurations likely coexisting at room temperature.

On the other hand, the structure of Na_{0.5}Mn_{0.75}PS₃ · 2 H₂O contains no bridging H₂O ligands. The H₂O coordinates to Na⁺ and participates in hydrogen bonding with nearby H₂O ligands. The higher density of H₂O molecules in Na_{0.5}Mn_{0.75}PS₃ · 2 H₂O forces the H₂O to distort in the *c* direction and results in roughly a bilayer structure in the *ab* plane, again supporting the experimentally observed $d_{(001)}$ spacing that suggests bilayer H₂O in the interlayer when two H₂O per formula unit are introduced. The $d_{(001)}$ spacing of the monolayer and bilayer relaxed structures are 8.9 Å and 10.3 Å respectively, which are smaller than the XRD measured values of 9.3 Å and 12.0 Å for K_{0.5}Mn_{0.75}PS₃ · H₂O

and Na_{0.5}Mn_{0.75}PS₃ · 2 H₂O, respectively, likely due to thermal expansion at room temperature compared to the calculated structure at 0 K.

Electrochemical Characterization of the Ionic Mobility

The elemental and structural analysis provides evidence that the intercalated ions are introduced into MPS₃ frameworks and occupy the interlayer space. These results are consistent with previous work on alkali metal ion-intercalated MPS₃ materials,^{43,45,52,58} and show that the concept is extendable to many other ions. Due to the increased bottleneck size in the migration pathway, as well as the screened Coulombic interactions between the interlayer cation and anion framework, we hypothesize that the intercalated ions should exhibit enhanced mobility.

To probe the ionics of the materials, the ionic conductivity and activation energy of all compounds is measured using EIS on cold-pressed pellets with a 6 mm diameter. The pellets are assembled in PTFE Swagelok cells with symmetric ion-blocking electrodes. For each material, EIS is measured at a range of temperatures from room temperature (RT) to 70 °C. Representative Nyquist plots for all compounds are shown in Figure S13 and S14, and an example of a fit using an equivalent circuit model for a sample where the high frequency semicircle can be resolved is shown in Figure S15. The E_a is determined using the well-established Arrhenius-type relationship that governs the thermally activated ionic conduction process.^{4,74} Figure S16 and S17 show average Arrhenius-type plots of $\ln(\sigma T)$ vs. T^{-1} for all studied ion-exchanged compounds. The σ_{RT} values and E_a for all studied compounds are plotted in Figure 4a and b, respectively. Figure 4a and b show the mean and standard deviations obtained from at least three replicate cells, each from a different synthesis batch, and these values are also listed in Table S1. In general, all of the compounds containing solvated ions in the interlayer show high total ionic conductivities at RT, and by 70 °C all exhibit practically useful conductivities > 0.1 mS cm⁻¹.

Detailed analysis of the dataset enabled by this modular framework facilitates the development structure-property relationships for ligand-coordinated ion conduction in rigid solids.

The Mobility of Various Ions in a Given Framework

The differences in performance between various ions in a given framework elucidates the effect of charge density and bottleneck size on mobility. It is evident that the ions with higher charge density generally exhibit a lower σ_{RT} and a higher E_a . Thus, the charge density of the mobile ion is a strong factor in determining its mobility, suggesting that the coordinating H₂O is not completely screening the charge. In an aqueous solution, ions with greater charge density attract more H₂O molecules to screen the charge. However, within a rigid solid framework, there is a limit to the number of H₂O molecules that can surround the ion due to spatial constraints. For example, Mg_{0.25}Cd_{0.75}PS₃ · 1.9 H₂O and Ca_{0.25}Cd_{0.75}PS₃ · 2 H₂O both contain bilayer H₂O and both have ~ 8 H₂O per cation. If the mobile ions migrate with the bound H₂O via a "vehicular mechanism" (discussed in detail later), the mobile complex to be considered is the $A^{n+} \cdot y \text{ H}_2\text{O}$ species. In this case, assuming each H₂O molecule provides the same degree of charge screening, the mobile complex Mg²⁺ · 8 H₂O is more charge-dense than the Ca²⁺ · 8 H₂O complex. Alternatively, if

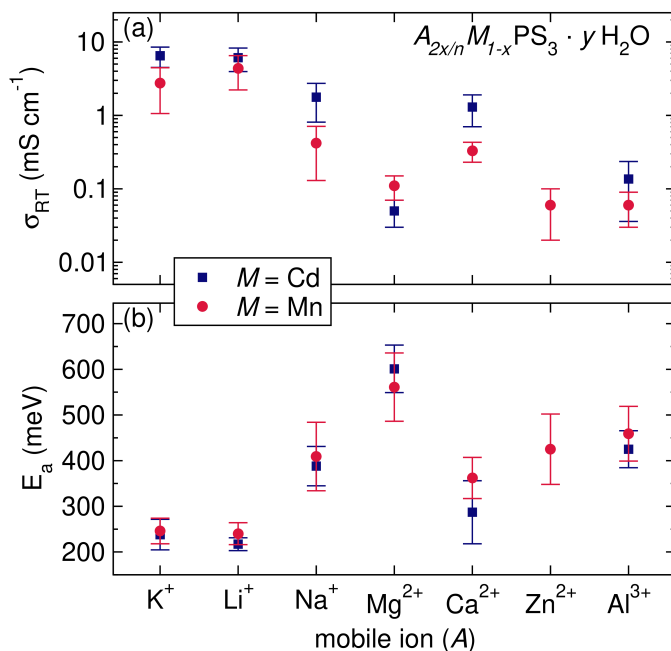


Figure 4. (a) The room temperature ionic conductivity (σ_{RT}) and (b) activation energy (E_a) of all ion-intercalated materials at ambient RH. $\text{Zn}_{0.4}\text{Cd}_{0.6}\text{PS}_3 \cdot 0.25 \text{H}_2\text{O}$ is not shown here because the σ_{RT} is too low ($10^{-9} \text{ S cm}^{-1}$).

the mobile ions conduct via a hopping mechanism between H_2O molecules the charge density differences between the cations must still be considered.

Furthermore, the charge density of the intercalated ion will affect the size of the hydrated complex and therefore also change the interlayer spacing. The migration bottleneck in these materials is essentially the interlayer spacing, which is directly related to the change in $d_{(001)}$. $\text{Mg}^{2+} - \text{OH}_2$ bonds are stronger than the $\text{Ca}^{2+} - \text{OH}_2$ bonds, as indicated by the higher peak mass loss temperature observed in TGA and DTG analyses (Figure S3). The stronger bond in the $\text{Mg}^{2+} \cdot 8 \text{H}_2\text{O}$ complex pulls the H_2O molecules closer to the cation, leading to less layer expansion and thus a more narrow bottleneck in $\text{Mg}_{0.25}\text{Cd}_{0.75}\text{PS}_3 \cdot 1.9 \text{H}_2\text{O}$ compared to $\text{Ca}_{0.25}\text{Cd}_{0.75}\text{PS}_3 \cdot 2 \text{H}_2\text{O}$. Again Al^{3+} is the outlier to this trend due to the excess water absorption, as discussed previously.

The combination of the higher charge density of the mobile complex and a narrower bottleneck explains the lower mobility of the charge-dense ions. These trends hold when comparing Na^+ and K^+ in the monolayer structures as well (Figure S18).

The Ionic Mobility Differences Between Frameworks

In most cases, the performance of a given ion between frameworks is similar (K^+ , Li^+ , Mg^{2+} , and Al^{3+}). In these cases, slight differences in performance between the two frameworks can be understood in the context of bottleneck size. The MnPS_3 -based Zn -intercalated compound exhibits significantly better performance than the CdPS_3 analogue, while the MnPS_3 -based compounds for Na^+ and Ca^{2+} ions both perform notably worse than the CdPS_3 analogue. Exploring these pronounced differences between frameworks allows us to highlight the impact of ligand-coordinated interlayer ions, the hydration state, and the charge screening by coordinated ligands.

The Effect of Diffusion Bottleneck Size. In the cases where

the frameworks have similar performance for a given ion, K^+ , Li^+ , Na^+ , Mg^{2+} , and Al^{3+} , the subtle differences can be explained by considering the bottleneck size. In the framework with the wider bottleneck, the σ_{RT} is slightly higher and E_a is slightly lower. As discussed previously, typically the CdPS_3 -based framework has the larger bottleneck and thus we observe that most ion-exchanged CdPS_3 phases have higher σ_{RT} and lower E_a than the MnPS_3 analogues. The exception is again the Mg^{2+} intercalated compounds, which show the opposite trend in $d_{(001)}$ spacing. This is reflected in the higher σ_{RT} and lower E_a for the MnPS_3 host compared to CdPS_3 . The observed trend in performance highlights the impact of bottleneck size on ion mobility, with larger bottlenecks facilitating improved ion transport.

The Effect of Ligand-Coordinated Interlayer Ions. The σ_{RT} of $\text{Zn}_{0.4}\text{Cd}_{0.6}\text{PS}_3$ is on the order of $10^{-9} \text{ S cm}^{-1}$ (not shown in Figure 4), which is four orders of magnitude lower than that of $\text{Zn}_{0.6}\text{Mn}_{0.4}\text{PS}_3$. The superior performance of $\text{Zn}_{0.6}\text{Mn}_{0.4}\text{PS}_3$ is due to the presence of some hydrated Zn^{2+} ions in the van der Waals gap, whereas in $\text{Zn}_{0.4}\text{Cd}_{0.6}\text{PS}_3$ the Zn^{2+} ions are immobilized in the metal-layer lattice sites. This illustrates that the solvated interlayer cations are crucial to achieve high ionic conductivity.

The Effect of Hydration State. The disparity in Na^+ performance can be explained by the fact that $\text{Na}_{0.6}\text{Mn}_{0.7}\text{PS}_3 \cdot 1.6 \text{H}_2\text{O}$ is a two phase mixture of the monolayer and bilayer hydrated structures. The monolayer structure will have a much lower Na^+ mobility than the bilayer structure due to the decreased bottleneck size and less effective charge screening (this is discussed in detail in the SI). The performance of $\text{Na}_{0.6}\text{Mn}_{0.7}\text{PS}_3 \cdot 1.6 \text{H}_2\text{O}$ reflects the combined properties of both hydration states. By equilibrating the material at 75 % RH, the bilayer structure ($\text{Na}_{0.6}\text{Mn}_{0.7}\text{PS}_3 \cdot 2 \text{H}_2\text{O}$) can be isolated. $\text{Na}_{0.6}\text{Mn}_{0.7}\text{PS}_3 \cdot 2 \text{H}_2\text{O}$ exhibits a conductivity more similar to that of $\text{Na}_{0.5}\text{Cd}_{0.75}\text{PS}_3 \cdot 2 \text{H}_2\text{O}$ as expected (Figure S18).

The Effect of Charge Screening with Ligand Molecules. Similarly to the Na -containing frameworks, $\text{Ca}_{0.25}\text{Mn}_{0.75}\text{PS}_3 \cdot 1.5 \text{H}_2\text{O}$ absorbs less H_2O than $\text{Ca}_{0.25}\text{Cd}_{0.75}\text{PS}_3 \cdot 2 \text{H}_2\text{O}$ at ambient RH. However, despite the lower H_2O content, the layer spacing associated with the bilayer phase is maintained and does not collapse to the monolayer structure. Instead, we assume the solvation shells around the Ca^{2+} ions in the MnPS_3 host are incomplete relative to the CdPS_3 host at ambient RH. The maintenance of a bilayer H_2O structure despite H_2O loss allows us to isolate the effect of charge screening from the impact of bottleneck size. Clearly, the difference in H_2O content and solvation significantly impacts the ionic conduction, as evidenced by the 25% higher E_a in $\text{Ca}_{0.25}\text{Mn}_{0.75}\text{PS}_3 \cdot 1.5 \text{H}_2\text{O}$ (362 meV) compared to $\text{Ca}_{0.25}\text{Cd}_{0.75}\text{PS}_3 \cdot 2 \text{H}_2\text{O}$ (287 meV). Notably, the $\text{Ca}_{0.25}\text{Mn}_{0.75}\text{PS}_3 \cdot 1.5 \text{H}_2\text{O}$ also contains 25% less water compared to $\text{Ca}_{0.25}\text{Cd}_{0.75}\text{PS}_3 \cdot 2 \text{H}_2\text{O}$. Therefore, the E_a increase and corresponding σ_{RT} decrease in the Mn -based framework is attributed to the less effective screening of Ca^{2+} in $\text{Ca}_{0.25}\text{Mn}_{0.75}\text{PS}_3 \cdot 1.5 \text{H}_2\text{O}$ due to the lower H_2O per cation. This highlights the crucial role of charge screening in facilitating high ionic mobility in MPS_3 frameworks.

Identification of the Mobile Ion

Though we can draw several structure-property relationships using the range of materials discussed above while assuming the charge carriers are primarily the hydrated cations, the use of H_2O as the coordinating ligand introduces the possibility of H^+ conduction. It has long been debated whether the ionic conductivity of ion-intercalated hydrated clays is a result of primarily H^+ conduction or migration of the intercalated ions.^{28–30,68} Therefore, care must

be taken to identify the majority charge carrier in $A_{2x/n}M_{1-x}PS_3 \cdot y H_2O$ materials.

Mobile H^+ in $A_{2x/n}M_{1-x}PS_3 \cdot y H_2O$ could potentially arise through either surface acidity,⁷⁵ or hydrolysis of H_2O bound to intercalated cations that act as Lewis bases.^{29,30} Since S-based materials tend to adsorb less surface H_2O than O-based materials, due to weaker hydrogen bonds between H_2O and S, surface acidity likely plays a less significant role in MPS_3 -based frameworks than in clays. To estimate the contribution of H^+ from surface acidity to the total conductivity, we investigate the ionic conductivity of pure MPS_3 phases under ambient relative humidity (the EIS results are shown in Figure S19). The σ_{RT} of $MnPS_3$ and $CdPS_3$ are 3×10^{-9} and $4 \times 10^{-10} S cm^{-1}$, respectively, which is four or five orders of magnitude lower than that of the worst performing $A_{2x/n}M_{1-x}PS_3 \cdot y H_2O$ compounds. Therefore, the observed ionic conductivity in $A_{2x/n}M_{1-x}PS_3 \cdot y H_2O$ materials is likely either due to mobile H^+ from the acidity of the ion-solvating H_2O or due to the conduction of the interlayer cations themselves.

Several characteristics of $A_{2x/n}M_{1-x}PS_3 \cdot y H_2O$ suggest that the intercalated cations are the majority charge carriers. The fact that the ions are able to be inserted and removed by ion exchange in an aqueous solution indicates their inherent mobility within the structure. Additionally, the absence of superstructure peaks at low Q regions of the XRD patterns suggests that the intercalated ions are not ordered and thus points to the ions' high mobility.⁷² Furthermore, the strong correlation between the E_a and σ_{RT} with the identity of the intercalated ion underscores the importance of these ions on charge transport. The E_a for H^+ conduction through a Grotthuss type mechanism, where H^+ are being exchanged by neighboring H_2O molecules, is typically $< 400 meV$.^{63,65} The variation in E_a measured in the materials reported here is between 216 and 622 meV, which is more consistent with the conduction of mobile complexes of different charge densities, as discussed above. The observed trends in σ_{RT} also do not align with H^+ being the majority charge carrier. The H^+ concentration would depend on the acidity of the absorbed H_2O , which is influenced by the charge density of the intercalated cation. Therefore, the trend in pK_a of the hydrated cations can be used to predict the trend in H^+ concentration in $A_{2x/n}M_{1-x}PS_3 \cdot y H_2O$. In general, the more charge-dense the cation, the more acidic the bound H_2O will be due to A-O bond strength. The pK_a trend of the intercalated ions is overlaid onto the σ_{RT} data in Figure S20. The $A_{2x/n}M_{1-x}PS_3 \cdot y H_2O$ compounds with more acidic interlayer ions (e.g. Mg^{2+} , Zn^{2+} , Al^{3+}) should have the highest H^+ concentration but show the lowest measured ionic conductivities. Thus the observed electrochemical performance is not adequately explained by assuming H^+ is the majority charge carrier.

Ionic Mobility Characterization with MAS NMR

We employ MAS NMR to directly probe the ionic mobility in $A_{2x/n}Cd_{1-x}PS_3 \cdot y H_2O$. Performing MAS NMR measurements on $MnPS_3$ -based compounds is challenging due to the presence of paramagnetic Mn^{2+} , however, we anticipate that the results of the $CdPS_3$ -based compounds can be extended to the $MnPS_3$ -based analogues.

Figure 5a shows 1H MAS NMR spectra of all $A_{2x/n}Cd_{1-x}PS_3 \cdot y H_2O$ materials to explore the dynamics of H_2O or H^+ . The chemical shifts of the central band are provided next to the corresponding spectra, and are listed in Table S2 along with the FWHM of the spectra.

For the $A_{2x/n}Cd_{1-x}PS_3 \cdot y H_2O$ compounds, the 1H NMR spectra all contain a single resonance appearing within a very narrow range of resonant frequencies, indicating a single 1H environ-

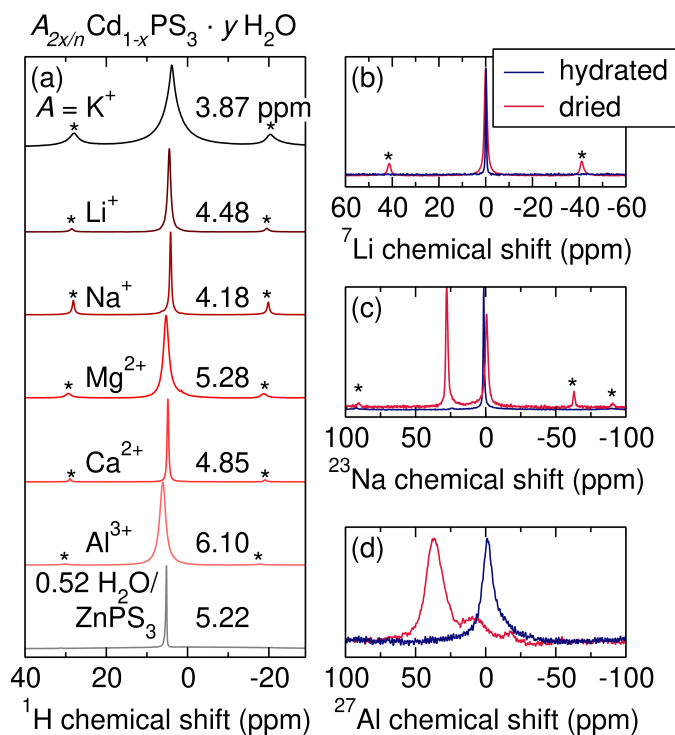


Figure 5. MAS NMR study of $A_{2x/n}Cd_{1-x}PS_3 \cdot y H_2O$ materials. (a) 1H MAS NMR spectra of $A_{2x/n}Cd_{1-x}PS_3 \cdot y H_2O$ compounds and $0.52 H_2O/ZnPS_3$ for comparison. (b) 7Li spectra of $Li_{0.5}Cd_{0.75}PS_3 \cdot 2 H_2O$, (c) ^{23}Na spectra of $Na_{0.5}Cd_{0.75}PS_3 \cdot 2 H_2O$, and (d) ^{27}Al MAS NMR spectra of $Al_{0.17}Cd_{0.75}PS_3 \cdot 2.3 H_2O$. The metal MAS NMR spectra are collected on the materials at ambient RH (hydrated), and after drying under vacuum at $200^\circ C$ for ≈ 10 hours (dried). * marks the spinning sidebands.

ment or that all 1H environments are exchanging faster than the NMR timescale in each compound. The observed chemical shifts are within the range expected for H in H_2O molecules (around 5 ppm),⁷⁶⁻⁷⁹ but are noticeably shifted and broader than the signal of "bulk" free H_2O , which is characterized by a sharp peak at ~ 4.75 ppm.^{80,81} The 1H chemical shift values trend with the charge density of the intercalated cation. Cations with higher charge density experience stronger interactions with the O in H_2O and are thus stronger bases, resulting in more deshielded hydrogen nuclei. Even though $Al_{0.17}Cd_{0.75}PS_3 \cdot 2.3 H_2O$ has more H_2O than can fit directly around each Al^{3+} ion in the bilayer structure, the NMR spectrum suggests that this excess water is not free. There is potentially a second "shell" of H_2O around the Al^{3+} ions in the interlayer. Exchange of the H_2O in the first and second shell could result in averaging of the H environments into the broad signal that we observe in Figure 5a. In general, these results indicate that the H_2O molecules in $A_{2x/n}Cd_{1-x}PS_3 \cdot y H_2O$ are bound to the intercalated cations, in agreement with the TGA results.

Additionally, narrow line widths are typically indicative of high H^+ mobility in inorganic solid materials that contain H_2O ;^{37,78,79,82} however, all $A_{2x/n}Cd_{1-x}PS_3 \cdot y H_2O$ materials exhibit relatively broad line widths. A relevant material to compare the line widths to is H_2O -exposed $ZnPS_3$, which is denoted as $0.52 H_2O/ZnPS_3$ in Figure 5a. When $ZnPS_3$ is exposed to humid air, the H_2O adsorbs at the grain boundaries resulting in solvation of Zn^{2+} into confined water environments yielding mobile Zn^{2+} , however, the H^+ are also mobile and account for roughly 50% of the charge carriers.³⁷ Notably, the line widths measured for the $A_{2x/n}Cd_{1-x}PS_3 \cdot y H_2O$ materials are much broader suggesting less mobile H^+ . Additionally, the appearance of spinning sidebands in the 1H NMR

spectra of $A_{2x/n}Cd_{1-x}PS_3 \cdot y H_2O$ materials further underlines that the H^+/H_2O molecules are bound to the cations and exhibit limited mobility.

We can additionally evaluate the mobility of the intercalated cations for NMR-active nuclei. Figure 5b, c, and d show 7Li , ^{23}Na , and ^{27}Al MAS NMR spectra, respectively, in both hydrated and dehydrated states in order to probe the mobility of the intercalated cations with and without H_2O ligands. The comparison between the hydrated and dehydrated materials can be found in the next subsection. The 7Li and ^{23}Na MAS NMR spectra of the respective hydrated ion-intercalated $CdPS_3$ samples both show narrow line widths and an absence of spinning sidebands, suggesting that the cations are sufficiently mobile to average out anisotropic interactions. The chemical shifts for Li and Na are 0.1 ppm and 1.34 ppm, respectively, which are consistent with previous reports of interlayer ions in bilayer H_2O -containing hydrated structures of $Li_2Sn_2S_5$ and Na-containing mica clays.^{36,83,84} The ^{23}Na spectrum of the hydrated phase is consistent with previous ^{23}Na MAS NMR studies on $Na_{0.50}Cd_{0.75}PS_3 \cdot 2 H_2O$,^{58,60} which postulated that the Na^+ ions likely conduct with the bound H_2O molecules in the interlayer.

In the case of $Al_{0.17}Cd_{0.75}PS_3 \cdot 2.3 H_2O$, the ^{27}Al MAS NMR spectrum contains a single resonance at -1.5 ppm which is consistent with Al^{3+} that is octahedrally coordinated by H_2O (~ 0 ppm).^{85,86} The broader line width is consistent with the lower mobility of Al^{3+} but could also be related to quadrupolar effects due to the potential asymmetry of the coordination environment in the interlayer.

The observed correlation between electrochemical properties and the intercalated ions strongly suggests that the ionic mobility observed in all of these compounds is predominantly due to the intercalated ions. Furthermore, this claim is supported by the lack of evidence for rapid H^+ exchange, along with the clear indications of metal ion mobility from our NMR studies of the selected ions (7Li , ^{23}Na , and ^{27}Al). Note, conducting metal cation NMR analyses on the K^+ , Mg^{2+} , Ca^{2+} and Zn^{2+} materials is prohibitively challenging due to the low natural abundance of their NMR-active isotopes and quadrupolar effects.

Mechanistic Investigation of Ionic Conduction with PFG NMR

To determine if the ionic conduction mechanism is associated with a hopping vs. vehicular mechanism, we use 7Li and 1H PFG NMR to directly measure the diffusivity and E_a of Li and H in $Li_{0.5}Cd_{0.75}PS_3 \cdot 2 H_2O$. The normalized echo signal attenuation data obtained by PFG NMR are best fit to a biexponential for both 7Li and 1H (Figure S21). The Tanner-Stejskal equation^{87,88} used to analyze the results assumes an isotropic diffusion process, which is justified here given the polycrystalline nature and morphology of the particles, and presumable lack of preferred orientation of individual crystallites. Hence, we rule out the possibility of having two different diffusing species/pathways in the ab plane, or different in-plane diffusivity (in the ab plane) compared to the out-of-plane diffusivity (c direction), and instead suggest that the presence of two $^1H/^7Li$ diffusing components results from nuclei primarily diffusing within a grain, or at or across a grain boundary during the measurement. A two component model also best captured the behavior observed in a PFG NMR study of hydrated $Li_2Sn_2S_5$ by Joos *et al.*³⁶ In that study, the authors suggested it was likely due to in-plane vs. out-of-plane diffusion in hydrated $Li_2Sn_2S_5$, but also did not rule out grain boundary contributions.

Figure 6 shows Arrhenius-type plots of $\ln(D)$ vs. $1000/T$ for both the Li- and H-containing species, where D is the diffusivity of the diffusing components. The room temperature diffusivities of the Li

components are 1.62×10^{-10} and $3.09 \times 10^{-11} m^2 s^{-1}$, which is associated with 57% and 43% of the Li species measured, respectively. The diffusivities of the H species are 1.13×10^{-12} and $1.55 \times 10^{-14} m^2 s^{-1}$, which is associated with 18% and 82% of the H species, respectively. The second, low diffusivity component is not shown in Figure 6b. Since the Li diffusivity is a few orders of magnitude higher than that of H, we can deduce that Li are the majority charge carriers and that the Li^+ conduct through a hopping mechanism between H_2O molecules, instead of a vehicular mechanism in which Li^+ conducts with its solvation shell. Interestingly, this mechanism is in contrast to that suggested in case of hydrated $Li_2Sn_2S_5$ in which the Li and H diffusivities were comparable leading to the conclusion of a vehicular ionic conduction mechanism.³⁶

The E_a can be obtained from the Arrhenius-type plots in Figure 6. The PFG NMR determined E_a for Li diffusion are 180 and 150 meV for component one and two, respectively. These E_a values are consistent to that measured by EIS (217 ± 14 meV). The E_a measured for the H-containing component is even lower than the Li components at 120 meV, though we note this value is more of an estimate due to the low measured diffusivity. Though the E_a for the H-containing component is low, the much lower diffusivity suggests that the majority charge carrier measured with EIS is Li.

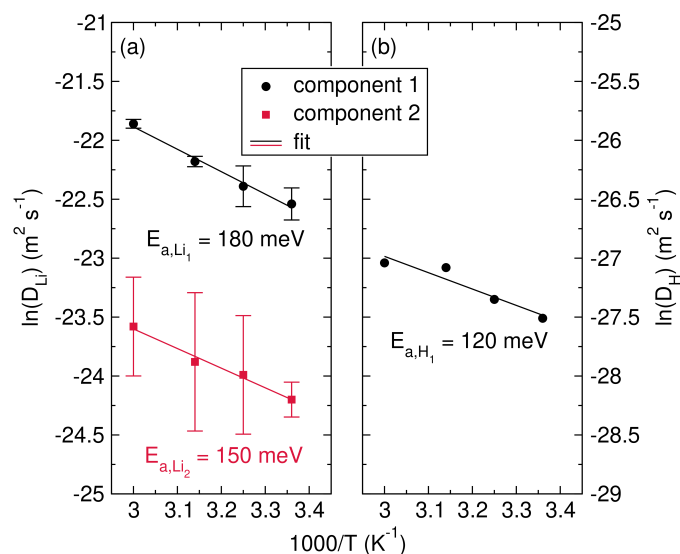


Figure 6. Arrhenius-type relationships of the diffusivity (D) measured with (a) 7Li and (b) 1H PFG NMR. The second component of associated with the H-containing species is not shown due to the low diffusivity.

Structural and Electrochemical Characterization of Dried $A_{2x/n}Cd_{1-x}PS_3$

Although the primary charge carriers are likely the intercalated ions rather than mobile H^+ , the H_2O ligands play a critical role in enabling the high conductivity. We use MAS NMR and XRD to investigate the local and long-range structural changes that occur after drying in a vacuum oven at $T \geq 100^\circ C$ for at least 10 hours, and EIS to probe the electrochemical performance.

The XRD patterns of $A_{2x/n}Cd_{1-x}PS_3$ pre- and post-drying are shown in Figure S22. Lattice contraction is observed after drying all samples. For the majority of the dry samples, the basal spacing resembles that of the pristine $CdPS_3$ phase. Only dried $K_{0.5}Cd_{0.75}PS_3$ and $Na_{0.5}Cd_{0.75}PS_3$ materials display a larger basal spacing than the pristine $CdPS_3$ material.

The removal of the majority of water in the dried $A_{2x/n}Cd_{1-x}PS_3$

$\cdot y \text{H}_2\text{O}$ compounds is confirmed by the significant reduction of the ^1H signal (an example is shown in Figure S23).

Without H_2O , the intercalated cations are destabilized within the van der Waals gap, causing them to occupy the vacant M sites. This has been shown previously for Li^+ -intercalated MnPS_3 ,⁵² as well as A^{3+} -ion intercalated CdPS_3 .⁸⁹ For monovalent ions, there are twice as many intercalated ions as there are vacancies in the metal layer, therefore at least half of the ions may remain trapped in the van der Waals gap. In the case of K -intercalated MPS_3 , the K^+ is too large to occupy the vacant sites in the metal layer, and therefore all of the K^+ likely remains in the van der Waals gap. This is evidenced by the lack of a reflection resembling the pristine material lattice spacing in dried $\text{K}_{0.5}\text{Cd}_{0.75}\text{PS}_3$, and is supported by DFT structural calculations discussed in the Supporting Information. In the case of dried $\text{Na}_{0.5}\text{Cd}_{0.75}\text{PS}_3$, the XRD pattern shows a reflection corresponding to the spacing of pristine CdPS_3 in addition to a reflection indicating a slightly expanded lattice. The ^{23}Na MAS NMR of dried $\text{Na}_{0.5}\text{Cd}_{0.75}\text{PS}_3$, shown in Figure 5c, contains two distinctive resonances which could be assigned to even distributions of Na in two different chemical environments. The ^{23}Na spectrum of dried $\text{Na}_{0.5}\text{Cd}_{0.75}\text{PS}_3$ strongly resembles the ^{23}Na spectrum of $\text{Na}_4\text{P}_2\text{S}_6$.⁹⁰ The -0.7 ppm resonance likely corresponds to the interlayer Na^+ and the 27.7 ppm resonance is attributed to the Na^+ that occupies the metal layer. These values are slightly different than $\text{Na}_4\text{P}_2\text{S}_6$ (5.6 ppm and 18.2 ppm respectively) due to the structural and chemical changes imparted by the Cd ions in $\text{Na}_{0.5}\text{Cd}_{0.75}\text{PS}_3$.

Although 0.25 equivalents of Li^+ likely remains in the van der Waals gap in dried $\text{Li}_{0.5}\text{Cd}_{0.75}\text{PS}_3$,⁵² layer expansion is not observed because Li is small enough to occupy the interlayer without expanding the $d_{(001)}$ spacing, as is the case in $\text{Li}_4\text{P}_2\text{S}_6$. However, typically ^7Li MAS NMR does not permit differentiation between the different chemical environments.^{91–93}

For multivalent ion intercalated samples, no layer expansion is observed in the dried materials because the number of intercalated ions is less than or equal to the number of vacancies, so all of the ions occupy the metal layer. As evidenced in Figure 5d, after drying, the ^{27}Al resonance shifts to 36 ppm, which is more reminiscent of Al octahedrally coordinated by S .⁸⁶

The dried multivalent-intercalated compounds do not exhibit any meaningful ionic conductivity ($< 10^{-9} \text{ S cm}^{-1}$), however the remnant interlayer monovalent ions in the dried monovalent-intercalated compounds enable the study of metal cation mobility in MPS_3 frameworks in the absence of solvating ligands. Notably, the ^7Li and ^{23}Na MAS NMR spectra show broadening of the signals and emergence of spinning sidebands after drying, indicating reduced mobility.

Figure 7a shows the basal spacing of $\text{A}_{2x/n}\text{Cd}_{1-x}\text{PS}_3$ ($\text{A} = \text{Li}, \text{Na}, \text{K}$) pre- and post-drying. In contrast to the hydrated phases, where the basal spacing is determined firstly by the amount of H_2O absorbed and secondly by the charge density of the ion and by extension the size of the hydrated complex, the $d_{(001)}$ spacing of the dried phases trends with the intercalated ionic radius. In the absence of the bottleneck expansion and charge screening, the σ_{RT} drops by up to six orders of magnitude, and the E_a increases up to three-fold. In this case, the trend in electrochemical behavior is in line with what is expected of traditional solid state electrolytes. $\text{Li}_{0.5}\text{Cd}_{0.75}\text{PS}_3$ exhibits the highest conductivity, due to the inherent mobility of the small, low charge density Li^+ cation.

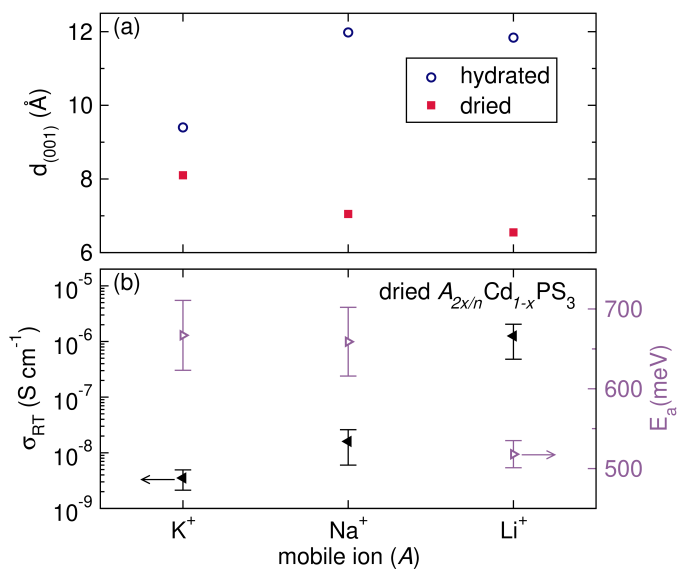


Figure 7. (a) The $d_{(001)}$ spacing of monovalent-ion intercalated CdPS_3 in the hydrated and dried state, and (b) σ_{RT} and E_a of dried monovalent ion-intercalated CdPS_3 .

Ligand Exchange of $\text{A}_{2x/n}\text{M}_{1-x}\text{PS}_3 \cdot y \text{H}_2\text{O}$

The absorbed H_2O ligands are vital for enabling high ionic mobility. However, in many battery systems, H_2O can cause undesired side reactions that impair performance. To extend the applicability of these materials to non-aqueous systems, the H_2O can be replaced with more stable organic molecules. Further, the ligand exchange helps to elucidate the effect of the ligands on ionic conduction, specifically by comparing the impact of opening the diffusion bottleneck and the degree of charge screening. As a proof of concept we exchange H_2O ligands for other solvent molecules that are frequently used in next-generation battery liquid electrolytes: MeCN and THF. These molecules cover a range of dielectric constants, as shown in Figure 8a, allowing us to further probe the effect of charge screening.

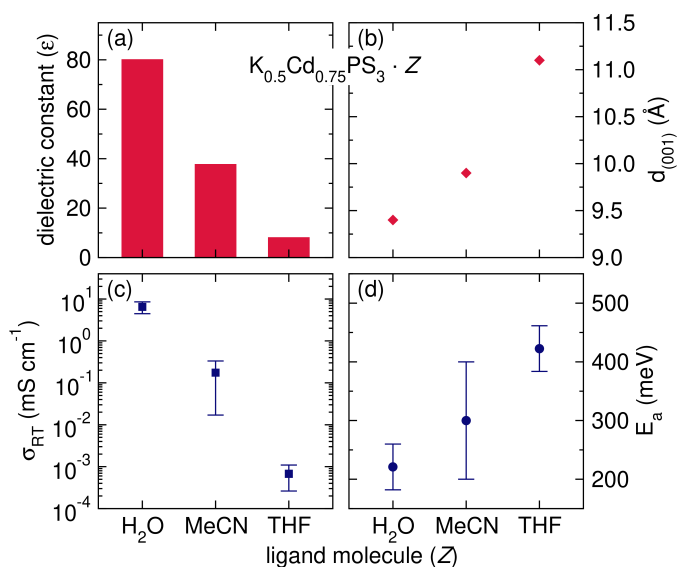


Figure 8. (a) A bar chart showing the reported dielectric constants of H_2O , MeCN, and THF, and comparisons of (b) $d_{(001)}$, (c) σ_{RT} , and (d) E_a of $\text{K}_{0.5}\text{Cd}_{0.75}\text{PS}_3 \cdot Z$ ($Z = \text{H}_2\text{O}, \text{MeCN}, \text{or THF}$).

The solvent exchange is done by first exposing $K_{0.5}Cd_{0.75}PS_3$ to vacuum to at least partially dry the material followed by stirring the $K_{0.5}Cd_{0.75}PS_3$ in dried solvent in a glovebox for 1 h. To confirm that the organic solvent is incorporated, Raman is measured on the resulting materials. In all cases, the Raman modes associated with the new ligand are observed (Figure S23). To further confirm ligand exchange, we analyze the basal spacing after the exchange which is shown in Figure 8b (XRD patterns available in Figure S24). The basal spacing increases in the order of $H_2O < MeCN < THF$, correlating with the size of the ligand molecules. The increase in basal spacing with THF (4.5 Å) approximately matches the radius of a flat THF molecule (4.2 Å).⁹⁴ Figure 8c and d show the σ_{RT} and E_a , respectively, of $K_{0.5}Cd_{0.75}PS_3 \cdot Z$ ($Z = H_2O, MeCN, THF$). Replacing H_2O with MeCN or THF decreases the σ_{RT} by one or three orders of magnitude and increases the E_a by ~ 70 meV or 200 meV, respectively. Given that the framework and mobile ion remain constant, the variation in mobility is attributed to the interplay between an increase in bottleneck size and decrease in the extent of charge screening. Despite THF creating the largest diffusion bottleneck as evidenced by the basal spacing, the THF-containing compounds show low σ_{RT} and high E_a due to either ineffective charge screening by THF or a bottleneck that is effectively too large. However, the conductivity with adsorbed THF is still two orders of magnitude higher than dried $K_{0.5}Cd_{0.75}PS_3$. Although MeCN adsorption results in a smaller bottleneck than THF, its superiority in terms of screening the mobile ion charge leads to a significantly higher σ_{RT} and lower E_a . The variation in dielectric constant of the selected ligands (53 % decrease for MeCN, 90 % decrease for THF) is larger than the resulting variation in bottleneck size (5 % increase for MeCN, 18 % increase for THF). Therefore, the variation in screening ability plays the dominant role in governing the mobility. Consequently, $K_{0.5}Cd_{0.75}PS_3 \cdot MeCN$ exhibits a high ionic conductivity of 0.18 mS cm^{-1} in the absence of H_2O , enabling potential application in non-aqueous systems. In addition, achieving high ionic conductivity with an aprotic ligand provides further evidence that the majority charge carriers are the interlayer cations and not H^+ . Future work will explore the integration of aprotic solvents with high dielectric constants into MPS_3 frameworks with various next-generation mobile ions.

Ionic Conduction in $A_{2x/n}M_{1-x}PS_3$ Compared to Previous Reports

Now that we have discussed in-depth the structure-property relationships associated with ionic conduction in the $A_{2x/n}M_{1-x}PS_3$ materials, we will next discuss our work in the context of similar studies.

In the late 90s, Jeevanandam *et al.* measured ionic conductivity using admittance measurements of $K_{0.5}Cd_{0.75}PS_3 \cdot H_2O$ and $Na_{0.5}Cd_{0.75}PS_3 \cdot 2 H_2O$.^{58,59} The studies concluded that Na^+ is mobile while K^+ is not. However, the EIS analysis presented here conclusively shows very high ionic conductivity for K^+ in $K_{0.5}Cd_{0.75}PS_3 \cdot H_2O$ (Nyquist plots can be seen in Figure S13). Additionally, we find that the σ_{RT} of $Na_{0.5}Cd_{0.75}PS_3 \cdot 2 H_2O$ is two orders of magnitude higher than in their previous reports. These discrepancies may arise from sample preparation or EIS measurement errors, but it is difficult to pinpoint the exact cause using the experimental conditions that were reported.

The recent study by Yu and Ren, in which exceedingly high 2D ionic conductivity was observed in $CdPS_3$ -based membranes, provides an opportunity to compare solvent-assisted ionic conductivity to confined liquid electrolytes. In the study by Yu and Ren, there

is no discussion of the quantity of H_2O present in each membrane. However, since the basal spacing, σ_{RT} , and E_a are largely uncorrelated to the identity of the intercalated ion, reminiscent of a confined liquid electrolyte we speculate that the membranes likely contain excess amounts of H_2O . In the case of ligand-assisted ionic conduction in bulk $A_{2x/n}M_{1-x}PS_3$ materials, although the intercalated ions are screened they still interact with the framework, explaining the strong dependence of the electrochemical performance on intercalated ion identity. A comparison of the results of their 2D σ_{RT} and E_a with the finding of this study is shown in Figure S26. The measured conductivity of $CdPS_3$ -based membranes is between two and four orders of magnitude higher than the bulk polycrystalline $A_{2x/n}M_{1-x}PS_3$ samples reported here. This is logical because the inherent conduction pathways in this structure are 2D, bulk 3D conduction is achieved in polycrystalline pellets through a series of 2D conduction processes within randomly oriented particles. However, particularly for energy storage applications considering general materials processing and cell assembly steps, the bulk 3D measurement is more representative of materials performance. Furthermore, operating within the ligand-assisted regime combines the benefits of high ionic mobility with the advantages of using a solid state electrolyte. Additionally, there is limited free H_2O in the material, which minimizes H_2O -related undesired side reactions, and limits the impact of H^+ conduction. However, in the confined liquid electrolyte regime the materials may become softer and sticky due to excess H_2O ,³⁶ and the free H_2O can lead to undesired reactivity and increased H^+ conduction in battery systems.

Conclusions

The introduction of ligand molecules into solids can drastically increase the ionic mobility of both larger cations (Na^+ , K^+ , Ca^{2+}) and charge-dense cations (Mg^{2+} , Zn^{2+} , Al^{3+}) by expanding the diffusion bottlenecks and screening charge-dense mobile ions. In MPS_3 -based materials ($M = Mn, Cd$), ion-intercalated compounds of the form $A_{2x/n}M_{1-x}PS_3 \cdot y H_2O$ can be obtained containing hydrated interlayer A cations. These intercalated structures contain either a monolayer H_2O , K^+ and Na^+ (at low RH); or bilayer H_2O : Li^+ , Na^+ , Mg^{2+} , Zn^{2+} , Ca^{2+} , and Al^{3+} , depending on the hydration energy of the intercalated cation. All $A_{2x/n}M_{1-x}PS_3 \cdot y H_2O$ materials show exceptionally high bulk conductivity (generally $> 0.1 \text{ mS cm}^{-1}$) at RT and ambient RH. Therefore, leveraging ligand-assisted ionic conduction in solid state electrolytes is a promising avenue to achieving high ionic mobility of next-generation mobile ions, which has historically been very challenging.^{36,38,39,95,96} Furthermore, $A_{2x/n}M_{1-x}PS_3 \cdot y H_2O$ materials display the highest reported bulk conductivity of any electronically-insulating inorganic solid for K^+ , Mg^{2+} , Ca^{2+} , Al^{3+} ions, and is among the highest for Li^+ and Na^+ . Notably, these compounds exhibit higher conductivities than other reported solids containing solvated ions (e.g. clays and MOFs), due in part to the more polarizable S-based anion framework in MPS_3 -based materials. Employing ligand-assisted ionic conduction seems to be more effective for achieving exceedingly high conductivity for less charge-dense ions, like Li^+ , Na^+ , K^+ , and Ca^{2+} , but still provides suitable results for charge-dense ions.

This work highlights the impact of expanding the diffusion bottleneck, by showing that with identical ions and ligands the framework with the larger bottleneck has a higher σ_{RT} and lower E_a . Furthermore, the impact of charge screening is illustrated by the systematic increase in E_a and decrease in σ_{RT} for similar structures when some of the solvating H_2O ligands are removed.

Since the introduction of H_2O introduces the possibility of H^+

conduction, we provide strong evidence that the intercalated cations are the majority carriers. The observed electrochemical behavior is much more adequately explained by mobile intercalated ions than mobile H^+ . Additionally, MAS NMR demonstrates absence of H^+ exchange and high mobility of Li^+ and Na^+ . PFG NMR demonstrates that in the case of $Li_{0.5}Cd_{0.75}PS_3 \cdot 2 H_2O$ the Li diffusivity is two to four orders of magnitude higher than that of H. This result further suggests that the intercalated cation is the majority charge carrier and that the conduction occurs through a hopping mechanism, where the cations are moving between H_2O molecules, instead of a vehicular mechanism.

Although H^+ are likely not the mobile ions, the drastically inferior performance of the dried phases emphasizes that H_2O ligands are crucial for the high mobility of the intercalated ions. Finally, exchanging H_2O for aprotic ligands like MeCN and THF in $K_{0.5}Cd_{0.75}PS_3 \cdot H_2O$ provides further evidence that H^+ is not the majority carrier. The ionic mobility of the intercalated cations with these ligands depends on the interplay between bottleneck expansion and the effective charge screening. Specifically, $K_{0.5}Cd_{0.75}PS_3 \cdot MeCN$ exhibits a high ionic conductivity demonstrating the potential application of $A_{2x/n}M_{1-x}PS_3$ to non-aqueous systems.

$A_{2x/n}M_{1-x}PS_3$ materials represent a modular system in which we can change the mobile ion, the framework ($M = Cd$ for slightly higher performance vs. Mn for environmental friendliness), or the ligand molecules to tailor the performance for specific applications. Fundamentally, this modular framework allows us to develop structure property relationships to better understand solid state ionic conduction of next-generation mobile ions, particularly solvent-assisted ionic conduction. Additionally, the high performance of $A_{2x/n}M_{1-x}PS_3$ materials suggests that these, or similar compounds, could be used as a "universal" solid electrolyte for a variety of battery chemistries with different mobile ions.

Experimental Methods

Material Preparation

Synthesis

The MPS_3 ($M = Mn, Cd$) materials were prepared using traditional solid state methods from Mn (Alfa Aesar, 99.3%) or Cd (Thermo Scientific, 99.99%) metal powder, respectively, elemental S (Acros Organics, >99.5%), and 10% excess P_2S_5 (Acros Organics, >98%) in an Ar-filled glovebox without further purification.

The M , P_2S_5 , and S_8 were combined in a 2:1.1:1/8 molar ratio and ground thoroughly using a mortar and pestle. The reactants were then pressed into pellets with an Arbor press and sealed in a vitreous silica ampule under vacuum (<10 mtorr). The reaction vessel was placed in a box furnace, heated to 650 °C at a rate of 1 °C min^{-1} (K min^{-1}) and allowed to react at 650 °C for 24 h. After the reaction was complete, the tube was allowed to cool to ambient temperature inside of the furnace. The resulting green ($MnPS_3$) or off-white ($CdPS_3$) powder was collected and handled in an Ar filled glovebox.

Ion-Exchange Reaction

The ion-exchange reactions were conducted by stirring powder MPS_3 samples in aqueous solution of the appropriate metal chloride. A typical K-exchange reaction involved stirring 400 mg of $MnPS_3$ or 500 mg of $CdPS_3$ in 10 ml of a 3 M or 2 M solution, respectively, of aqueous KCl at room temperature for three hours. For $CdPS_3$, 0.1 M EDTA, in a 1 M $K_2CO_3/KHCO_3$ buffer solution,

is added as a complexing agent. After the reaction was complete, the mixture was filtered using a fritted glass vacuum filter, washed three times with water and once with ethanol and allowed to dry for at least 30 minutes. The second ion exchanges were conducted on the material obtained from the first exchange. In this case, 100-150 mg of K-exchanged MPS_3 was added to 10 ml of 1 M solutions of the relevant metal chloride, no complexing agents were added. The drying and washing procedures were the same as the first exchange. The Li-exchanged samples were allowed to dry overnight. After the ion exchanges were complete the samples were stored in vials at ambient conditions. A hygrometer was used to measure the ambient RH, if there was a period in which the humidity was < 40%, the materials were stored in a humidity chamber maintained at 53% RH using super saturated solutions of magnesium nitrate.

Ligand-Exchange Reaction

The ligand exchange was carried out in a dry N_2 -filled glove box. Samples of $K_{0.5}Cd_{0.75}PS_3 \cdot H_2O$ were partially dried through three 10-minute vacuum-backfill cycles in the glovebox antechamber. MeCN (99.9%, Fisher Scientific) and THF (99.9%, Fischer Scientific) were dried on a solvent purification system (Pure Process Technology) and transferred into the glovebox, without exposure to air, and stored over 3 Å molecular sieves. Before use, the measured a water content of both solvents was less than 20 ppm via KF titration. In the glovebox, $K_{0.5}Cd_{0.75}PS_3$ was added to 5 mL of the solvent in a scintillation vial and mixed on a magnetic stir plate for one hour. The mixture was vacuum filtered over a fritted glass filter for a couple seconds until the material visibly changed from its dark gray "wet" state to the drier light gray state. Quickly, the material was scraped off the filter and put into Swagelok cells for impedance characterization or an empty scintillation vial for absorbed solvent characterization.

Absorbed solvent was characterized by mass loss measurements. An initial mass was obtained from the sample immediately following removal from the filter. This sample was then allowed to passively lose solvent to the dry atmosphere.

Dried Sample

To prepare dried ion-exchanged materials for structural and electrochemical characterization, the powders were transferred into a Ar-filled glovebox and placed in a vacuum oven at 120 °C for 10 hours.

Pelletization

Between 15-30 mg of powder was pressed into a pellet in ambient atmosphere using a 12 ton hydraulic press from Carver (unit 3912). The powder was pressed using a 6 mm stainless steel die set at 2 tons for 5 minutes. The resulting pellets were between 0.2-0.6 mm thick. In most cases the pellets were sputtered with Au at 40 mA for 60 s on both flat surfaces using a Ted Pella 108 Auto Sputter Coater in an Ar filled glovebox. Then removed from the glovebox and allowed to re-equilibrate at ambient RH for at least 2 days.

Material Characterization

Powder X-ray Diffraction

High-resolution synchrotron powder x-ray diffraction patterns were collected on samples sealed in 1.0 mm (o.d) glass capillaries (to prevent changes in RH). The samples were measured on beamline 28-ID-1 ($\lambda = 0.1665$ Å) at the National Synchrotron Light Source II at Brookhaven National Laboratory.

Additional XRD data were collected using a Rigaku SmartLab diffractometer (CuK α). The hydrated samples were placed on a glass slide sample holder at ambient RH, while the dried samples were prepared in a glovebox and measured in a Rigaku air free sample holder. All patterns were collected from 5-60° 2 θ as a step size of 0.03° and 5° per minute.

Raman Spectroscopy

Raman spectroscopy was measured using a Horiba Instruments XplorRA PLUS Raman Spectrometer equipped with 532 nm laser. The sample was mounted on a glass microscope slide. The signal was averaged over 200 acquisitions lasting 1 s each with a 50 μ m slit and 500 μ m hole. The laser power used was either 1 or 10% to prevent local heating and sample degradation.

Thermogravimetric Analysis

TGA was performed using a TA Instruments TGA 550. Powder samples (5-30 mg) were loaded into a tared high-temperature pan composed of an Inconel coated bail wire and platinum pan as a flat, evenly distributed layer and heated under a nitrogen flow (25 mL/min) at 5° C/min from room temperature (19-25° C) to 200° C, at which it was held constant for 1 min. The instrument was calibrated using a nickel Curie temperature standard as per the manufacturer's directions.

Inductively Coupled Plasma Mass Spectrometry

ICP-MS was performed on Agilent 8800. About 2 mg of each synthesized batch of material was digested in 2 ml of 70% nitric acid at 80° C for 4 hours. After the initial digestion, the solutions were diluted twice in 5% nitric acid to reach x2500 dilution. Five different concentrations of standard solutions were made from stock solutions of Cd, Mn, P, S, Li, Na, Mg, Ca, Zn, and Al to generate a calibration curve.

Scanning Electron Microscopy & Energy Dispersive X-ray Spectroscopy

SEM was performed on select materials using a ZEISS 1550VP field emission SEM with an acceleration voltage of 10 kV at 5kX, 10kX, and 30kX magnification. Before SEM was performed the materials were sputtered with Pt for 5 s at 40 mA to avoid charging during the measurement. EDS data were collected using an Oxford X-MAX SSD system with an acceleration voltage of 10 kV or 20 kV.

Electrochemical Impedance Spectroscopy

EIS measurements were collected using a Bio-Logic VSP300 multichannel potentiostat with ultralow current probes. Typically, symmetric cells were assembled with Au-sputtered, in 0.25 i.d. PTFE spring-loaded Swagelok cells. EIS was measured at different temperatures, controlled by a convection oven. The cell temperature was allowed to equilibrate for 30 minutes at each temperature. The temperature series were terminated at 70° C. The EIS spectra were collected using a sinusoidal voltage amplitude of 50 mV in a frequency range of 3 MHz to 1 Hz and averaged over 10 measurements. At least three successive measurements were taken to ensure that the response was stable. Equivalent results were obtained without pelletization, by making a pellet *in situ* in the PTFE Swagelok cell by applying at least 3 kN of force with a vice. In this case, either polished Au foil or the stainless steel plungers were used as electrodes. This method was primarily utilized for the Al-exchanged

samples, which took a long time to re-equilibrate after pelletization, it was also used for replicates of other samples to ensure consistency. Since for the vast majority of samples the high frequency semi circle in the Nyquist plot could not be resolved even at RT, the x intercept of the Nyquist plot is taken as a "worst case" approximation for the total impedance for all samples, which we conservatively approximate as the electrolyte impedance. For the few samples where a high frequency semi-circle could be resolved, the data were fit to an equivalent circuit using ZFit in the EC-Lab software, e.g. Figure S15, to ensure that the capacitance of this feature corresponded with that expected for bulk ionic conductivity in solids.

Solid State Magic Angle Spinning Nuclear Magnetic Resonance Spectroscopy

Multinuclear MAS NMR experiments were performed using a Bruker Avance I-500 MHz spectrometer and using a Bruker 4mm MAS NMR probe. A powder sample was packed into a zirconia (ZrO₂) rotor at the ambient condition, and spun at 10 kHz. ¹H NMR (500.2 MHz) spectra were acquired after 4 μ s-90 degree pulse. NMR signal of metal ions (quadrupole nuclei) were recorded after applying short tip angle rf pulses (1/12 π for I=3/2 nuclei (⁷Li and ²³Na) or 1/18 π pulse for ²⁷Al) and strong ¹H decoupling pulse. Chemical shifts were externally calibrated to TMS for ¹H, 1 M aqueous solution of LiCl, NaCl, and Al(NO₃) for ⁷Li, ²³Na, and ²⁷Al nuclei, respectively. For NMR measurements after dehydration, a 4 mm rotor containing packed powder sample was inserted into a 80 mm long-5 mm glass NMR tube, and the glass NMR tube was attached to a 1/4"-Cajon-VCR-T fitting and the side arm was connected to a vacuum manifold for high temperature evacuation overnight. In this special setup, a glass rod with sealing kel-F rotor cap at the end was attached at the top of the 1/4"-Cajon-VCR-T. The rod was able to slide down, closing the 4 mm rotor with a tightly fit o-ring. The rotor underwent heating in an 10 mm-cylinder furnace with evacuation. The setup was filled with Ar gas before sealing, resulting in complete avoidance of exposure to air for the dried powder sample.

Pulsed Field Gradient Nuclear Magnetic Resonance Spectroscopy

Li_{0.5}Cd_{0.5}PS₃ · 2 H₂O sample was packed and sealed inside a 4 mm ZrO₂ rotor, which was itself placed in an airtight 5 mm NMR tube. ¹H and ⁷Li PFG-NMR measurements were conducted on a 7.05 T (¹H, 300 MHz) Bruker Avance III super wide-bore NMR spectrometer equipped with a Diff50 probe under static condition. Diffusion measurements were performed from low (25° C) to high temperature (60° C) after a 30 minute equilibration period at each temperature, and the temperature was regulated by a heater and using N₂ gas flowing at a rate of 800 L/h. The sample temperature was calibrated using dry ethylene glycol solution. Self-diffusion coefficients were measured using a stimulated echo pulse sequence⁸⁷ with variable magnetic field gradient pulses. Self-diffusion coefficients, D_i , of all the nuclei were determined by fitting the integrated signal intensity, I_i , as a function of the variable gradient strength, g , using the Stejskal-Tanner equation.^{88,97}

$$I = I_0 \exp \left(-D_i (\gamma \delta g)^2 \left(\Delta - \frac{\delta}{3} \right) \right) = I_0 \exp (-D_i B) \quad (3)$$

where $B = (\gamma \delta g)^2 \left(\Delta - \frac{\delta}{3} \right)$

I_0 is the initial signal intensity, δ is the gradient duration, and Δ is the diffusion time. The δ , Δ , and g values were selected to

ensure sufficient decay window. The NMR data were processed with TOPSPIN 4.3.0 and fitted using Origin software.

Theoretical Methods

Structure Relaxations

We used density functional theory implemented in the Vienna Ab Initio Simulation Package (VASP 6.4.2)^{98–100} along with Projector Augmented Wave (PAW)^{101,102} pseudopotentials to determine the lowest energy configurations of dehydrated and hydrated $K_{0.5}Mn_{0.75}PS_3$ and $Na_{0.5}Mn_{0.75}PS_3$. The stoichiometries were rounded to the stated values for computational simplicity. PAW potentials were used with valence configurations of $3s^23p^64s^1$ for K, $2s^22p^4$ for O, $3s^23p^3$ for P, $3s^23p^4$ for S, $4s^13d^6$ for Mn and $1s^1$ for H to describe the valence electrons. Our calculations employed the Perdew-Burke-Ernzerhof (PBE)¹⁰³ Generalized Gradient Approximation (GGA) and included vdW corrected DFT-D3 (Becke-Johnson)^{104,105} along with empirical dispersion corrections. To ensure accuracy, we included all plane waves of energy up to 650 eV and set electronic minimization energy criteria to 10^{-6} eV. Ionic relaxation was stopped when the norms of all Hellmann-Feynman forces were less than $10^{-2}/\text{\AA}$, and we utilized a $4 \times 2 \times 4$ Γ -centered k-mesh for Brillouin zone integration within the unit cells so that a k-spacing of less than 0.2\AA^{-1} was sufficient for the required accuracy for electronic energy minimization.

The structures in Figure 3 were obtained through a heating and cooling approach using Ab initio Molecular Dynamics (AIMD) and the Nosé and Hoover NVT ensemble in VASP 6.4.2.^{106–109} The structures were brought from 20K to 300K, held at 300K then cooled back to 20K and were relaxed with DFT minimization from there. Initial estimate structures were optimized with the parameters described above. All AIMD simulations were run with 1 fs time steps, a fixed cell shape and volume, and the same parameters above except as noted. The heating and cooling were both performed over 2 ps with a $1 \times 1 \times 1$ Γ -centered k-mesh. Between these steps the simulation was held at 300 K over 5 ps with a $2 \times 1 \times 2$ Γ -centered k-mesh.

Supporting Information

Details on the differences in the degree of ion exchange that occurs, both for different ions within a given framework and between the frameworks; additional details of the ligand exchange procedure, challenges, and results; additional XRD, EIS, Arrhenius relationships, TGA, DTG, Raman, SEM, EDS of MPS_3 -based intercalated compounds; XRD of select compounds at different RH; additional computational structural investigations of $K_{0.5}Mn_{0.75}PS_3 \cdot H_2O$; EIS of pristine MPS_3 materials; XRD of dried MPS_3 -based ion exchanged compounds; MAS NMR of select compounds in hydrated and dried states; XRD and Raman of compounds after ligand exchange; a comparison between electrochemical results of ligand-assisted ionic conduction and a confined liquid electrolyte; Tables containing the electrochemical properties of each sample and the chemical shifts and FWHM from MAS NMR.

Acknowledgment

This research was supported by the Arnold and Mabel Beckman Foundation through the Beckman Young Investigator Award. The authors also acknowledge support from the Packard Fellowship for Science and Engineering, the Alfred P. Sloan Foundation, and the

Camille and Henry Dreyfus Foundation. The ICP-MS data were collected at the Water and Environment Lab at Caltech. The authors thank Dr. Nathan Dalleska for assistance with ICP-MS sample preparation and data collection. The authors thank Michelle Qian and Gihan Kwon for assistance preparing samples for and measuring synchrotron XRD. S.S. thanks the UCLA-Caltech Medical Scientist Training Program (MSTP) through the National Institutes of Health (NIH) NIGMS training grant T32 GM008042 for support. The work of TD and WAG was supported by the Hong Kong Quantum AI Lab, AIR@InnoHK of Hong Kong Government.

References

- (1) Grey, C. P.; Tarascon, J. M. Sustainability and in Situ Monitoring in Battery Development. *Nature Mater* **2017**, *16*, 45–56.
- (2) Olivetti, E. A.; Ceder, G.; Gaustad, G. G.; Fu, X. Lithium-Ion Battery Supply Chain Considerations: Analysis of Potential Bottlenecks in Critical Metals. *Joule* **2017**, *1*, 229–243.
- (3) Sun, X.; Hao, H.; Hartmann, P.; Liu, Z.; Zhao, F. Supply Risks of Lithium-Ion Battery Materials: An Entire Supply Chain Estimation. *Materials Today Energy* **2019**, *14*, 100347.
- (4) Iton, Z. W. B.; See, K. A. Multivalent Ion Conduction in Inorganic Solids. *Chem. Mater.* **2022**, *34*, 881–898.
- (5) Lundgren, C. A.; Murray, R. W. Observations on the Composition of Prussian Blue Films and Their Electrochemistry. *Inorg. Chem.* **1988**, *27*, 933–939.
- (6) Itaya, K.; Uchida, I.; Neff, V. D. Electrochemistry of Polynuclear Transition Metal Cyanides: Prussian Blue and Its Analogues. *Acc. Chem. Res.* **1986**, *19*, 162–168.
- (7) Lee, H.-W.; Wang, R. Y.; Pasta, M.; Woo Lee, S.; Liu, N.; Cui, Y. Manganese Hexacyanomanganate Open Framework as a High-Capacity Positive Electrode Material for Sodium-Ion Batteries. *Nat Commun* **2014**, *5*, 5280.
- (8) Farrington, G. Divalent Beta''-Aluminas: High Conductivity Solid Electrolytes for Divalent Cations. *Solid State Ionics* **1982**, *7*, 267–281.
- (9) Kummer, J. β -Alumina Electrolytes. *Progress in Solid State Chemistry* **1972**, *7*, 141–175.
- (10) Yung-Fang Yu Yao.; Kummer, J. Ion Exchange Properties of and Rates of Ionic Diffusion in Beta-Alumina. *Journal of Inorganic and Nuclear Chemistry* **1967**, *29*, 2453–2475.
- (11) Whittingham, M. S.; Huggins, R. A. Measurement of Sodium Ion Transport in Beta Alumina Using Reversible Solid Electrodes. *The Journal of Chemical Physics* **1971**, *54*, 414–416.
- (12) Goodenough, J.; Hong, H.-P.; Kafalas, J. Fast Na^+ -Ion Transport in Skeleton Structures. *Materials Research Bulletin* **1976**, *11*, 203–220.
- (13) Pal, S. K.; Saha, R.; Kumar, G. V.; Omar, S. Designing High Ionic Conducting NASICON-type $Na_3Zr_2Si_3PO_{12}$ Solid-Electrolytes for Na-Ion Batteries. *J. Phys. Chem. C* **2020**, *124*, 9161–9169.
- (14) Guin, M.; Tietz, F.; Guillon, O. New Promising NASICON Material as Solid Electrolyte for Sodium-Ion Batteries: Correlation between Composition, Crystal Structure and Ionic Conductivity of $Na_{3+x}Sc_2Si_xP_{3-x}O_{12}$. *Solid State Ionics* **2016**, *293*, 18–26.
- (15) Aurbach, D.; Lu, Z.; Schechter, A.; Gofer, Y.; Gizbar, H.; Turgeman, R.; Cohen, Y.; Moshkovich, M.; Levi, E. Prototype Systems for Rechargeable Magnesium Batteries. *Nature* **2000**, *407*, 724–727.
- (16) Sun, X.; Bonnick, P.; Nazar, L. F. Layered TiS_2 Positive Electrode for Mg Batteries. *ACS Energy Lett.* **2016**, *1*, 297–301.
- (17) Sun, X.; Bonnick, P.; Duffort, V.; Liu, M.; Rong, Z.; Persson, K. A.; Ceder, G.; Nazar, L. F. A High Capacity Thioisopinel Cathode for Mg Batteries. *Energy Environ. Sci.* **2016**, *9*, 2273–2277.
- (18) Canepa, P.; Bo, S.-H.; Sai Gautam, G.; Key, B.; Richards, W. D.; Shi, T.; Tian, Y.; Wang, Y.; Li, J.; Ceder, G. High Magnesium Mobility in Ternary Spinel Chalcogenides. *Nat Commun* **2017**, *8*, 1759.
- (19) Glaser, C.; Wei, Z.; Indris, S.; Klement, P.; Chatterjee, S.; Ehrenberg, H.; Zhao-Karger, Z.; Rohnke, M.; Janek, J. To Be or Not to Be – Is $MgSc_2Se_4$ a Mg-Ion Solid Electrolyte? *Advanced Energy Materials* **2023**, 2301980.
- (20) Martinolich, A. J.; Lee, C.-W.; Lu, I.-T.; Bevilacqua, S. C.; Preefer, M. B.; Bernardi, M.; Schleife, A.; See, K. A. Solid-State Divalent Ion Conduction in $ZnPS_3$. *Chem. Mater.* **2019**, *31*, 3652–3661.
- (21) Higashi, S.; Miwa, K.; Aoki, M.; Takechi, K. A Novel Inorganic Solid State Ion Conductor for Rechargeable Mg Batteries. *Chem. Commun.* **2014**, *50*, 1320–1322.
- (22) Yan, Y.; Grinderslev, J. B.; Jørgensen, M.; Skov, L. N.; Skibsted, J.; Jensen, T. R. Ammine Magnesium Borohydride Nanocomposites for All-Solid-State Magnesium Batteries. *ACS Appl. Energy Mater.* **2020**, *3*, 9264–9270.
- (23) Yan, Y.; Dononelli, W.; Jørgensen, M.; Grinderslev, J. B.; Lee, Y.-S.; Cho, Y. W.; Černý, R.; Hammer, B.; Jensen, T. R. The Mechanism of Mg^{2+} Conduction in Ammine Magnesium Borohydride Promoted by a Neutral Molecule. *Phys. Chem. Chem. Phys.* **2020**, *22*, 9204–9209.
- (24) Le Ruyet, R.; Fleutot, B.; Berthelot, R.; Benabed, Y.; Hautier, G.; Filinchuk, Y.; Janot, R. $Mg_3(BH_4)_4(NH_2)_2$ as Inorganic Solid Electrolyte with High Mg^{2+} Ionic Conductivity. *ACS Appl. Energy Mater.* **2020**, *3*, 6093–6097.
- (25) Kisu, K.; Kim, S.; Inukai, M.; Oguchi, H.; Takagi, S.; Orimo, S.-i. Magnesium Borohydride Ammonia Borane as a Magnesium Ionic Conductor. *ACS Appl. Energy Mater.* **2020**, *3*, 3174–3179.

- (26) Roedern, E.; Kühnel, R.-S.; Remhof, A.; Battaglia, C. Magnesium Ethylenediamine Borohydride as Solid-State Electrolyte for Magnesium Batteries. *Sci Rep* **2017**, *7*, 46189.
- (27) Whittingham, S. Transport Properties of the Mineral Vermiculite. *Solid State Ionics* **1989**, *32–33*, 344–349.
- (28) Whittingham, M. Sodium Ion Conduction in Single Crystal Vermiculite. *Solid State Ionics* **1987**, *25*, 295–300.
- (29) Maraqah, H.; Li, J.; Whittingham, M. S. Ion Transport in Single Crystals of the Clay-Like Aluminosilicate, Vermiculite. *MRS Proc.* **1990**, *210*, 351.
- (30) Slade, R. Conduction and Diffusion in Exchanged Montmorillonite Clays. *Solid State Ionics* **1987**, *24*, 289–295.
- (31) Ruiz-Hitzky, E.; Casal, B. Crown Ether Intercalations with Phyllosilicates. *Nature* **1978**, *276*, 596–597.
- (32) Nam, K. W. et al. The High Performance of Crystal Water Containing Manganese Birnessite Cathodes for Magnesium Batteries. *Nano Lett.* **2015**, *15*, 4071–4079.
- (33) Novák, P.; Desilvestro, J. Electrochemical Insertion of Magnesium in Metal Oxides and Sulfides from Aprotic Electrolytes. *J. Electrochem. Soc.* **1993**, *140*, 140–144.
- (34) Song, J.; Noked, M.; Gillette, E.; Duay, J.; Rubloff, G.; Lee, S. B. Activation of a MnO₂ Cathode by Water-Stimulated Mg²⁺ Insertion for a Magnesium Ion Battery. *Phys. Chem. Chem. Phys.* **2015**, *17*, 5256–5264.
- (35) Kundu, D.; Adams, B. D.; Duffort, V.; Vajargah, S. H.; Nazar, L. F. A High-Capacity and Long-Life Aqueous Rechargeable Zinc Battery Using a Metal Oxide Intercalation Cathode. *Nat Energy* **2016**, *1*, 16119.
- (36) Joos, M.; Schneider, C.; Münchinger, A.; Moudrakovski, I.; Usiskin, R.; Maier, J.; Lotsch, B. V. Impact of Hydration on Ion Transport in Li₂Sn₂S₅·xH₂O. *J. Mater. Chem. A* **2021**, *9*, 16532–16544.
- (37) Iton, Z. W. B.; Lee, B. C.; Jiang, A. Y.; Kim, S. S.; Brady, M. J.; Shaker, S.; See, K. A. Water Vapor Induced Superionic Conductivity in ZnPS₃. *J. Am. Chem. Soc.* **2023**, *145*, 13312–13325.
- (38) Yoshida, Y.; Yamada, T.; Jing, Y.; Toyao, T.; Shimizu, K.-i.; Sadakiyo, M. Super Mg²⁺ Conductivity around 10⁻³ Scm⁻¹ Observed in a Porous Metal–Organic Framework. *J. Am. Chem. Soc.* **2022**, *144*, 8669–8675.
- (39) Yoshida, Y.; Kato, K.; Sadakiyo, M. Vapor-Induced Superionic Conduction of Magnesium Ions in a Metal–Organic Framework. *J. Phys. Chem. C* **2021**, *125*, 21124–21130.
- (40) Park, S.; Kristanto, I.; Jung, G. Y.; Ahn, D. B.; Jeong, K.; Kwak, S. K.; Lee, S.-Y. A Single-Ion Conducting Covalent Organic Framework for Aqueous Rechargeable Zn-ion Batteries. *Chem. Sci.* **2020**, *11*, 11692–11698.
- (41) Miner, E. M.; Park, S. S.; Dincă, M. High Li⁺ and Mg²⁺ Conductivity in a Cu-Azolate Metal–Organic Framework. *J. Am. Chem. Soc.* **2019**, *141*, 4422–4427.
- (42) Iliescu, A.; Andrews, J. L.; Oppenheim, J. J.; Dincă, M. A Solid Zn-Ion Conductor from an All-Zinc Metal–Organic Framework Replete with Mobile Zn²⁺ Cations. *J. Am. Chem. Soc.* **2023**.
- (43) Clement, R. A Novel Route to Intercalation into Layered MnPS₃. *J. Chem. Soc., Chem. Commun.* **1980**, 647.
- (44) Whittingham, M. S. The Role of Ternary Phases in Cathode Reactions. *J. Electrochem. Soc.* **1976**, *123*, 315–320.
- (45) Clement, R.; Garnier, O.; Jegoudez, J. Coordination Chemistry of the Lamellar MPS₃ Materials: Metal-Ligand Cleavage as the Source of an Unusual "Cation-Transfer" Intercalation Process. *Inorg. Chem.* **1986**, *25*, 1404–1409.
- (46) Clément, R.; Lagadic, I.; Léaustic, A.; Audière, J. P.; Lomas, L. In *Chemical Physics of Intercalation II*; Bernier, P., Fischer, J. E., Roth, S., Solin, S. A., Eds.; Springer US: Boston, MA, 1993; Vol. 305; pp 315–324.
- (47) Fan, Y. A New Family of Fast Ion Conductor-Montmorillonites. *Solid State Ionics* **1997**, *93*, 347–354.
- (48) Suzuki, M.; Wada, N.; Hines, D.; Whittingham, M. S. Hydration States and Phase Transitions in Vermiculite Intercalation Compounds. *Phys. Rev. B* **1987**, *36*, 2844–2851.
- (49) Ouvrard, G.; Brec, R.; Rouxel, J. Structural Determination of Some MPS₃ Layered Phases (M = Mn, Fe, Co, Ni and Cd). *Materials Research Bulletin* **1985**, *20*, 1181–1189.
- (50) Shannon, R. D. Revised Effective Ionic Radii and Systematic Studies of Interatomic Distances in Halides and Chalcogenides. *Acta Cryst A* **1976**, *32*, 751–767.
- (51) Coradin, T.; Clément, R.; Lacroix, P. G.; Nakatani, K. From Intercalation to Aggregation: Nonlinear Optical Properties of Stilbazolium Chromophores-MPS₃ Layered Hybrid Materials. *Chem. Mater.* **1996**, *8*, 2153–2158.
- (52) Lagadic, I.; Lacroix, P. G.; Clément, R. Layered MPS₃ (M = Mn, Cd) Thin Films as Host Matrixes for Nonlinear Optical Material Processing. *Chem. Mater.* **1997**, *9*, 2004–2012.
- (53) Clement, R.; Léaustic, A.; Marney, K.; Francis, A. Synthesis and Luminescence Properties of CdPS₃ Intercalated with Rare Earth Cations. *Journal of Physics and Chemistry of Solids* **1994**, *55*, 9–16.
- (54) Coradin, T.; Coupé, A.; Livage, J. Intercalation of Biomolecules in the MnPS₃ Layered Phase. *J. Mater. Chem.* **2003**, *13*, 705–707.
- (55) Lagadic, I.; Léaustic, A.; Clément, R. Intercalation of Polyethers into the MPS₃ (M = Mn, Cd) Host Lattice. *J. Chem. Soc., Chem. Commun.* **1992**, *0*, 1396–1397.
- (56) Oriakhi, C. O.; Nafshun, R. L.; Lerner, M. M. Preparation of Nanocomposites of Linear Poly(Ethylenimine) with Layered Hosts. *Materials Research Bulletin* **1996**, *31*, 1513–1520.
- (57) Clement, R.; Lomas, L.; Audière, J. P. Intercalation Chemistry of Layered Iron Trithiophosphate (FePS₃). An Approach toward Insulating Magnets below 90 K. *Chem. Mater.* **1990**, *2*, 641–643.
- (58) Jeevanandam, P.; Vasudevan, S. Preparation and Characterization of Cd_{0.75}PS₃A_{0.5}(H₂O)_y [A=Na, K and Cs]. *Solid State Ionics* **1997**, *104*, 45–55.
- (59) Jeevanandam, P.; Vasudevan, S. Conductivity and Dielectric Response in the Ion-Exchange Intercalated Mono- and Double-Layer Hydrates Cd_{0.75}PS₃Na_{0.5}(H₂O)_y, y = 1, 2. *J. Phys. Chem. B* **1998**, *102*, 3082–3089.
- (60) Arun, N.; Jeevanandam, P.; Vasudevan, S.; Ramanathan, K. V. Motion of Interlamellar Hydrated Sodium Ions in Layered Cd_{0.75}PS₃Na_{0.5}(H₂O)₂. *The Journal of Chemical Physics* **1999**, *111*, 1231–1239.
- (61) Arun, N.; Vasudevan, S.; Ramanathan, K. V. Orientation and Motion of Interlamellar Water: An Infrared and NMR Investigation of Water in the Galleries of Layered Cd_{0.75}PS₃K_{0.5}(H₂O)_y. *J. Am. Chem. Soc.* **2000**, *122*, 6028–6038.
- (62) Ruiz-León, D.; Manríquez, V.; Kasaneva, J.; Avila, R. Insertion of Trivalent Cations in the Layered MPS₃ (Mn, Cd) Materials. *Materials Research Bulletin* **2002**, *37*, 981–989.
- (63) Qian, X.; Chen, L.; Yin, L.; Liu, Z.; Pei, S.; Li, F.; Hou, G.; Chen, S.; Song, L.; Thebo, K. H.; Cheng, H.-M.; Ren, W. CdPS₃ Nanosheets-Based Membrane with High Proton Conductivity Enabled by Cd Vacancies. *Science* **2020**, *370*, 596–600.
- (64) Yu, X.; Ren, W. 2D CdPS₃-Based Versatile Superionic Conductors. *Nat Commun* **2023**, *14*, 3998.
- (65) Agmon, N. The Grothuss Mechanism. *Chemical Physics Letters* **1995**, *244*, 456–462.
- (66) Hou, T.; Xu, W.; Pei, X.; Jiang, L.; Yaghi, O. M.; Persson, K. A. Ionic Conduction Mechanism and Design of Metal–Organic Framework Based Quasi-Solid-State Electrolytes. *J. Am. Chem. Soc.* **2022**, *144*, 13446–13450.
- (67) García, N. Conductivity in Na⁺- and Li⁺-Montmorillonite as a Function of Equilibrium Humidity. *Solid State Ionics* **1996**, *92*, 139–143.
- (68) Fan, Y. Cation Diffusion and Conduction in Solid Electrolytes Li, Na-montmorillonites. *Solid State Ionics* **1988**, *28–30*, 1596–1601.
- (69) Barj, M.; Lucazeau, G. Raman Spectra of Lamellar CdPS₃ Intercalated with Alkali Ions. *Solid State Ionics* **1983**, *9–10*, 475–479.
- (70) Schöllhorn, R.; Meyer, H. Cathodic Reduction of Layered Transition Metal Chalcogenides. *Materials Research Bulletin* **1974**, *9*, 1237–1245.
- (71) Lerb, A.; Schoellhorn, R. Solvation Reactions of Layered Ternary Sulfides A_xTi₂S₂, A_xNbS₂, and A_xTaS₂. *Inorg. Chem.* **1977**, *16*, 2950–2956.
- (72) Whittingham, M. The Hydrated Intercalation Complexes of the Layered Disulfides. *Materials Research Bulletin* **1974**, *9*, 1681–1689.
- (73) Ghidui, M.; Halim, J.; Kota, S.; Bish, D.; Gogotsi, Y.; Barsoum, M. W. Ion-Exchange and Cation Solvation Reactions in Ti₃C₂ MXene. *Chem. Mater.* **2016**, *28*, 3507–3514.
- (74) Famprikis, T.; Canepa, P.; Dawson, J. A.; Islam, M. S.; Masquelier, C. Fundamentals of Inorganic Solid-State Electrolytes for Batteries. *Nat. Mater.* **2019**, *18*, 1278–1291.
- (75) Frenkel, M. Surface Acidity of Montmorillonites. *Clays and Clay Minerals* **1974**, *22*, 435–441.
- (76) Hatz, A.-K.; Moudrakovski, I.; Bette, S.; Terban, M. W.; Etter, M.; Joos, M.; Vargas-Barbosa, N. M.; Dinnebier, R. E.; Lotsch, B. V. Fast Water-Assisted Lithium Ion Conduction in Restacked Lithium Tin Sulfide Nanosheets. *Chem. Mater.* **2021**, *33*, 7337–7349.
- (77) Ye, G.; Janzen, N.; Goward, G. R. Solid-State NMR Study of Two Classic Proton Conducting Polymers: Nafion and Sulfonated Poly(Ether Ether Ketone)s. *Macromolecules* **2006**, *39*, 3283–3290.
- (78) Ratcliffe, C.; Ripmeester, J.; Tse, J. NMR Chemical Shifts of Dilute ¹H in Inorganic Solids. *Chemical Physics Letters* **1985**, *120*, 427–432.
- (79) Volkov, V. I.; Chernyak, A. V.; Slesarenko, N. A.; Avilova, I. A. Ion and Molecular Transport in Solid Electrolytes Studied by NMR. *IJMS* **2022**, *23*, 5011.
- (80) Kwon, B. J. et al. High Voltage Mg-Ion Battery Cathode via a Solid Solution Cr–Mn Spinel Oxide. *Chem. Mater.* **2020**, *32*, 6577–6587.
- (81) Gun'ko, V. M.; Turov, V. V. Structure of Hydrogen Bonds and ¹H NMR Spectra of Water at the Interface of Oxides. *Langmuir* **1999**, *15*, 6405–6415.
- (82) Hayashi, S.; Mizuno, M. Proton Dynamics in Cs₂(HSO₄)(H₂PO₄) Studied by ¹H NMR. *Solid State Ionics* **2005**, *176*, 745–754.
- (83) Sanz, J.; Sobrados, I.; Robert, J.-L. Influence of Hydration on ²³Na, ²⁷Al, and ²⁹Si MAS-NMR Spectra of Sodium Saponites and Sodium Micas. *American Mineralogist* **2015**, *100*, 1076–1083.
- (84) Ohkubo, T.; Saito, K.; Kanehashi, K.; Ikeda, Y. A Study on Hydration Behaviors of Interlayer Cations in Montmorillonite by Solid State NMR. *Science and Technology of Advanced Materials* **2004**, *5*, 693–696.
- (85) Malicki, N.; Beccat, P.; Bourges, P.; Fernandez, C.; Quoineaud, A.-A.; Simon, L. J.; Thibault-Starzyk, F. *Studies in Surface Science and Catalysis*; Elsevier, 2007; Vol. 170; pp 762–770.
- (86) Haouas, M.; Taulelle, F.; Martineau, C. Recent Advances in Application of ²⁷Al NMR Spectroscopy to Materials Science. *Progress in Nuclear Magnetic Resonance Spectroscopy* **2016**, *94–95*, 11–36.
- (87) Tanner, J. E. Use of the Stimulated Echo in NMR Diffusion Studies. *The Journal of Chemical Physics* **1970**, *52*, 2523–2526.
- (88) Stejskal, E. O.; Tanner, J. E. Spin Diffusion Measurements: Spin Echoes in the Presence of a Time-Dependent Field Gradient. *The Journal of Chemical Physics* **1965**, *42*, 288–292.
- (89) Manríquez, V.; Galdámez, A.; Villanueva, A.; Aranda, P.; Galván, J. C.; Ruiz-Hitzky, E. Insertion of In(III) and Ga(III) into MPS₃ (M = Mn, Cd) Layered Materials. *Materials Research Bulletin* **1999**, *34*, 673–683.
- (90) Scholz, T.; Schneider, C.; Eger, R.; Duppel, V.; Moudrakovski, I.; Schulz, A.; Nuss, J.; Lotsch, B. V. Phase Formation through Synthetic Control: Polymorphism in the Sodium-Ion Solid Electrolyte Na₄P₂S₆. *J. Mater. Chem. A* **2021**, *9*, 8692–8703.
- (91) Haber, S.; Leskes, M. What Can We Learn from Solid State NMR on the Electrode–Electrolyte Interface? *Advanced Materials* **2018**, *30*, 1706496.

- (92) Ramsey, N. F. Magnetic Shielding of Nuclei in Molecules. *Phys. Rev.* **1950**, *78*, 699–703.
- (93) Komoroski, R. A. Applications of ^7Li NMR in Biomedicine. *Magnetic Resonance Imaging* **2000**, *18*, 103–116.
- (94) Beguin, F.; Setton, R.; Beguin, F.; Setton, R.; Hamwi, A.; Touzain, P. The Reversible Intercalation of Tetrahydrofuran in Some Graphite-Alkali Metal Lamellar Compounds. *Materials Science and Engineering* **1979**, *40*, 167–173.
- (95) Miner, E. M.; Dincă, M. Metal- and Covalent-Organic Frameworks as Solid-State Electrolytes for Metal-Ion Batteries. *Phil. Trans. R. Soc. A.* **2019**, *377*, 20180225.
- (96) Kharod, R. A.; Andrews, J. L.; Dincă, M. Teaching Metal-Organic Frameworks to Conduct: Ion and Electron Transport in Metal-Organic Frameworks. *Annu. Rev. Mater. Res.* **2022**, *52*, 103–128.
- (97) Sinnavee, D. The Stejskal–Tanner Equation Generalized for Any Gradient Shape—an Overview of Most Pulse Sequences Measuring Free Diffusion. *Concepts Magnetic Resonance* **2012**, *40A*, 39–65.
- (98) Kresse, G.; Hafner, J. *Ab Initio* Molecular Dynamics for Liquid Metals. *Phys. Rev. B* **1993**, *47*, 558–561.
- (99) Kresse, G.; Furthmüller, J. Efficiency of *Ab-Initio* Total Energy Calculations for Metals and Semiconductors Using a Plane-Wave Basis Set. *Computational Materials Science* **1996**, *6*, 15–50.
- (100) Kresse, G.; Furthmüller, J. Efficient Iterative Schemes for *Ab Initio* Total-Energy Calculations Using a Plane-Wave Basis Set. *Phys. Rev. B* **1996**, *54*, 11169–11186.
- (101) Kresse, G.; Joubert, D. From Ultrasoft Pseudopotentials to the Projector Augmented-Wave Method. *Phys. Rev. B* **1999**, *59*, 1758–1775.
- (102) Blöchl, P. E. Projector Augmented-Wave Method. *Phys. Rev. B* **1994**, *50*, 17953–17979.
- (103) Perdew, J. P.; Burke, K.; Ernzerhof, M. Generalized Gradient Approximation Made Simple. *Phys. Rev. Lett.* **1996**, *77*, 3865–3868.
- (104) Grimme, S.; Antony, J.; Ehrlich, S.; Krieg, H. A Consistent and Accurate *Ab Initio* Parametrization of Density Functional Dispersion Correction (DFT-D) for the 94 Elements H–Pt. *The Journal of Chemical Physics* **2010**, *132*, 154104.
- (105) Grimme, S.; Ehrlich, S.; Goerigk, L. Effect of the Damping Function in Dispersion Corrected Density Functional Theory. *J Comput Chem* **2011**, *32*, 1456–1465.
- (106) Nosé, S. A Unified Formulation of the Constant Temperature Molecular Dynamics Methods. *The Journal of Chemical Physics* **1984**, *81*, 511–519.
- (107) Nosé, S. Constant Temperature Molecular Dynamics Methods. *Prog. Theor. Phys. Suppl.* **1991**, *103*, 1–46.
- (108) Hoover, W. G. Canonical Dynamics: Equilibrium Phase-Space Distributions. *Phys. Rev. A* **1985**, *31*, 1695–1697.
- (109) Frenkel, D.; Smit, B. *Understanding Molecular Simulation*; Elsevier, 2002; pp 139–163.

TOC Graphic

